TRAVELING-WAVE LINBO3 OPTICAL MODULATOR USING Y-BRANCH DIRECTIONAL COUPLER

BY

CHANG MIN KIM

A DISSERTATION PRESENTED TO THE GRADUATE SCHOOL
OF THE UNIVERSITY OF FLORIDA IN PARTIAL FULFILLMENT
OF THE REQUIREMENTS FOR THE DEGREE OF
DOCTOR OF PHILOSOPHY

UNIVERSITY OF FLORIDA

1989

ACKNOWLEDGEMENTS

I wish to express my sincere appreciation to the chairman of my supervisory committee, Dr. M.V. Ramaswamy, for his expert guidance, encouragement, and support throughout this work. I would like to thank Drs. K. Srivastava, R. Zory, S.S. Li, and J. Simmons for their participation on my supervisory committee. I would like to express my thanks to Dr. P. Suchoski for his helpful advice in many regards. I would also like to thank Dr. S.Y. Wong of Hewlett Packard Laboratory for his cordial advice and assistance with microwave testing of the device.

I would like to express my thanks to J. Natour for the collaboration of a long and hard experiment, from fabrication to the measurement. I would also like to thank Mr. J. Chambliss for his assistance with the E-beam machine. I would like to thank S.S. Lee for helping me with the RF sputtering technique. I would also express my thanks to H.C. Cheng for his assistance with the use of the optical measurement set-up. Thanks are extended to my colleagues S.J. Lee, C. Rancoeil, Y.S. Kim, A. Milion, K. Slocumb and D. Lewis for many helpful discussions. Finally, I would like to thank Mr. M. Lewis for his assistance with file processing.

I am indebted to my mother for her support and sacrifice.

The financial support from MICROFABRITEC and DARPA is gratefully acknowledged.

TABLE OF CONTENTS

		PAGE
ACKNOWLEDGMENTS		ii
ABSTRACT		v
CHAPTERS		
1	INTRODUCTION	1
2	EFFECTIVE INDEX METHOD (EIM) AND EVALUATION OF ERROR	11
3	WKB ANALYSIS OF GUIDED-WAVE STRUCTURES	18
	WKB Theory	18
	Analysis of Graded-Index Channel Waveguides	26
	Analysis of Symmetric Directional Couplers	30
4	MODELING OF QUASI-TM GRADED-INDEX WAVEGUIDES	35
	2-D Finite Difference Method (2-D FDM)	37
	Modeling of Ti:$LiNbO_3$ Channel Waveguides	46
5	ELECTRODE ANALYSIS AND OVERLAP INTEGRAL FACTOR	55
	Conformal Mapping Technique for Electrode Analysis	56
	Overlap between RF Field and Optical Field	66
6	COUPLED MODE THEORY FOR Y-BRANCH DIRECTIONAL COUPLERS	74
	Uniform Directional Coupler	75
	Alternating $\Delta\beta$ Directional Coupler	79
	Y-branch Directional Coupler	82
7	TRAVELING-WAVE ELECTRODE AND MODULATION DEPTH	86
8	DESIGN AND FABRICATION OF Y-BRANCH OPTICAL MODULATORS	93
	Design of Y-branch Couplers and Electrodes	93
	Fabrication of $LiNbO_3$ Optical Modulators	96
9	MEASUREMENT AND RESULTS	102
10	SUMMARY AND DISCUSSION	108

APPENDICES

A CONFORMAL MAPPING FUNCTIONS 114

B PERTURBATION THEORY 117

REFERENCES 123

BIOGRAPHICAL SKETCH 128

Abstract of Dissertation Presented to the Graduate School
of the University of Florida in Partial Fulfillment of the
Requirements for the Degree of Doctor of Philosophy

TRAVELING-WAVE $LiNbO_3$ OPTICAL MODULATOR USING
Y-BRANCH DIRECTIONAL COUPLER

By

Chang Hie Kim

August 1982

Chairman: Ramu V. Ramaswamy
Major Department: Electrical Engineering

High-speed optical modulators are important components of wide-band single-mode optical communication systems. Such systems are very attractive for providing high capacity data links due to their small group velocity dispersion and low loss at 1.3 μm. Electrooptic external modulators using $LiNbO_3$ waveguides are potentially useful devices for high bit rate transmissions and signal processing.

Most intensity modulators are based on the theory of the uniform directional coupler. The traveling-wave electrodes are required to achieve the high-speed switching operation. There are a number of design parameters that determine the ultimate performance of Ti-indiffused $LiNbO_3$ modulators: namely, a good frequency response, a low switching voltage and a high extinction ratio. A trade-off is required depending on the parameter we emphasize.

We have developed several tools of theoretical analysis. These include the evaluation of the effective index method for step-index waveguides, new eigenvalue equations for the asymmetric directional coupler with graded-index profile using the WKB approach, nonuniform finite difference method

for modeling $LiNbO_3$ waveguides and electrode analysis by conformal mapping in the case of an anisotropic substrate. Additionally, we have analysed the frequency response of the traveling-wave electrode.

Based on the theoretical results obtained above, we designed a traveling-wave $LiNbO_3$ optical modulator using a Y-branch directional coupler. By employing the Y-branch directional coupler, we have reduced the device length by 30% as in comparison with the conventional uniform directional coupler. This enables us to achieve a device with large bandwidth. We have also designed a travelling-wave electrode of semi-infinite coplanar strip structure in order to achieve high-speed operation.

The dc test showed that the coupling length of the Y-directional coupler l_y was about 3.25 mm. The switching voltage of the device was nearly 12.5 V and the extinction ratio was 17 dB. We have fabricated two samples with coupling lengths of l_y and $0.75\ l_y$. The switching voltage and extinction ratio of the device of $0.75\ l_y$ were 20 V and 13 dB, respectively. Since we emphasized the large band-width, the device of $0.75\ l_y$ was chosen for the RF test at the cost of having a high switching voltage and a low extinction ratio. The projected band-width is around 25 GHz. The microwave test will be conducted in the near future.

CHAPTER 1

INTRODUCTION

Integrated optics has been an active research area for over two decades. Progress in the area of the optical switch/modulator has been significant in the last few years and is now at an advanced stage. The development in the integrated optics is strongly related to the rapid progress in low-loss, large bandwidth single mode fibers and semiconductor lasers. At the source end, a high speed modulator is needed to impress the electrical signal onto the lightwave carrier. Direct modulation of semiconductor lasers is efficient in the low-speed modulation area. However, this technique suffers from relaxation oscillation, spectral broadening and mixing phenomena in the case of high-speed modulation. Separation of the modulator from the spectrally pure laser source is necessary to achieve highly efficient modulation. This is especially true in coherent optical communications. External modulation/switching is accomplished through the refractive index change of the electro-optic material in the waveguide region by applying an external modulating electric field and modifying the propagation constant of the guided optical modes.

External modulators have been developed in both $LiNbO_3$ [1-5] and GaAs [6-10]. Initially, the poor material quality of GaAs gave rise to high insertion losses. The advent of new epitaxial growth techniques, such as MBE and MOCVD, has made it possible to fabricate optical devices with losses on the order of 0.2 dB/cm [11]. Since III-V materials offer the obvious

advantage of monolithic integration of photonic and electronic devices optimal modulators of these materials are the subjects of continuing research. Recently, a traveling-wave GaAs electrooptic waveguide modulator with a bandwidth in excess of 20 GHz has been achieved [10].

On the other hand $LiNbO_3$ has been widely used to fabricate low-loss (0.2 dB/cm) passive and active devices including optical waveguides and directional couplers [12] since the in-diffusion of Ti in $LiNbO_3$ results in an increase of the refractive index while maintaining the good electro-optic properties. Both Δn and the diffusion-length can be independently controlled by the Ti thickness, the diffusion time, and the diffusion temperature. Extensive studies of the refractive index profile, waveguide dispersion, and propagation loss in Ti $LiNbO_3$ have been reported [12-18]. A traveling-wave $LiNbO_3$ optical modulator using an asymmetric coplanar strip with a bandwidth of 22 GHz has been reported [19]. Comparison between GaAs and $LiNbO_3$ from the standpoint of modulation efficiency is illustrated as follows:

	$LiNbO_3$	GaAs
Microwave index ε_m	4.22	2.52
Optical index ε_o	2.15	3.42
Electro-optic coeff. r	30.8 x 10^{-12} m/V	1.2 x 10^{-12} m/V

The particular electro-optic effect for $LiNbO_3$ ($\varepsilon_o^3 r_{33} \sim 308 \times 10^{-12}$ m/V) is about 4.4 times higher than that of GaAs ($\varepsilon_o^3 r_{41} \sim 69 \times 10^{-12}$ e/V). However, a fair comparison must also include the bandwidth capability of the

travelling-wave modulators especially in terms of the velocity mismatch factor between the optical and RF signals [19-22]. The 3 dB bandwidth (BW) is inversely proportional to the mismatch factor $|v_m - v_o|$. These factors for $LiNbO_3$ and GaAs are 2.07 and 3.84 respectively, which means that the achievable BW of GaAs is higher than that of $LiNbO_3$ by a factor of about 2.5 for the same geometry of electrodes. This suggests that the electrode length L in GaAs can be 2.5 times larger than in $LiNbO_3$ for a given BW. We note that $\Delta\beta = (\epsilon^3 r)V_\pi L$. The voltage needed to induce a π phase shift, V_π, is one of the factors in determining the device's performance. Since this voltage is inversely proportional to the coupling length of the device, V_π for $LiNbO_3$ is 2.6 times smaller than that of GaAs for the same device dimension. The above discussion demonstrates that $LiNbO_3$ is a better choice for high-speed modulators using travelling-wave electrodes.

Several types of optical switches/modulators including the cut-off type, the uniform directional coupler, the Mach-Zehnder interferometer, the alternating $\Delta\beta$ directional coupler, the cross coupler, and the Y-branch directional coupler have been investigated. Brief pictures for each are illustrated in Fig. 1.

The cut-off modulator [23] is constructed to operate near cut-off for the fundamental mode. When an electric field is applied, the refractive index is changed, causing a change in the confinement of the optical field. A negative voltage will cause cut-off, resulting in loss of optical power in the form of radiation in the substrate and a positive voltage will result in a high confinement of the optical field. This kind of modulator is lossy since the waveguide operates near cut-off and is, therefore, not practical.

(a) Cut-off

(b) Uniform directional coupler (DC)

(c) Alternating Δβ DC

(d) Mach-Zehnder interferometer

(e) Cross coupler

(f) Y-branch DC

Fig 1.1 Types of optical modulators

The uniform directional coupler modulator [19-21] is one of the most widely used. Very high-speed devices are possible by combining this type with a traveling-wave electrode structure. The disadvantage of this type is that the extinction ratio of a device is degraded if the interaction length L of a device is not equal to the coupling length L_c, which requirement is rather difficult to achieve.

The Mach-Zehnder modulator [2-4] utilizes the phase difference in two waveguides by applying voltage to the push-pull electrodes. Two parallel waveguides are placed far enough apart so that there is no interaction between them. The performance of the device is not sensitive to the tolerance of the device dimension since phase construction or destruction can be easily controlled by changing the applied voltage. This type of modulator is not suitable for high-speed operation since the device needs to employ a complementary coplaner electrode structure, which makes it difficult to apply a traveling-wave modulating signal.

The alternating $\Delta\beta$ directional coupler modulator [24,25] is an extension of the uniform directional coupler. It has two separated electrodes with opposite polarities so that the coupling length can be controlled without changing the coupler dimension. Although this type of modulator does not require tight tolerance in the coupling length, it cannot be used for high-speed modulation since it is difficult to employ traveling-wave electrodes due to some restrictions. Typical restrictions are that the device length becomes twice as long as that of a uniform directional coupler type and that split microwave signal for each half electrode section needs to be out of phase.

The cross coupler modulator [26,27] is promising since it has a coupling length of the order of micrometers while other types have a coupling length of the order of millimeters. The physics of the switching phenomenon is that a given normal mode of the optical field tends to preserve itself while propagating as long as the adiabatic condition is satisfied while the other types make use of the beating of the fundamental and first order modes of the guiding structure. The electrode structure for the device is not suitable for traveling-wave application. This cross coupler device is useful for an optical switch rather than a modulator.

The Y-branch directional coupler modulator [5,28-30] is similar to the uniform directional coupler modulator except that it has a Y-junction in the input section. The input optical fields are always symmetric due to its symmetric optical waveguide structure. Due to this symmetry, the coupling length of the device can be reduced to almost 70% of that of the uniform directional coupler type [28]. This reduction in the dimension of the device makes it possible to achieve a higher bandwidth. This type of device is very promising for high-speed optical modulation despite the fact that the device is sensitive to the tolerances in the coupling length.

The performance of the optical modulators can be evaluated from several points of view such as high-speed, low applied voltage and high extinction ratio. The switching speed of the device is directly related to parameters such as the electro-optic coefficient of the material, velocity mismatch between the optical and traveling-wave RF signals (transit time difference), the impedance mismatch between the electrode and feeding/terminating sections, the electrode conductor loss and the device length. Specifically,

the device length varies exponentially with the channel gap. The applied voltage is also related to the electro-optic coefficient of the material, the overlap between the optical and modulating RF fields, the channel width and channel gap. The extinction ratio is a function of the given channel width and channel gap. It is difficult to find optimal parameters that provide high-speed (wide bandwidth), low applied voltage, and high extinction ratio all at the same time. For example, when we widen a channel gap to increase the extinction ratio, applied voltage increases accordingly, and the speed of a device deteriorates due to its increased sampling length.

This dissertation deals with the design consideration of a high-speed Y-branch modulator/switch and is organized as follows.

Chapters 2, 3, and 4 deal with the waveguide theory and modeling using several different methods.

In chapter 2, the effective index method (EIM) for step-index waveguides is described, and the pertinent error of the method is evaluated. The results of the EIM for a rectangular channel waveguide are compared with those of the 2-D finite difference method (FDM). It is shown that the results of the EIM are not suitable, near the cut-off region.

In chapter 3, WKB theory is used to obtain the pertinent eigenvalue equations for a single channel waveguide, symmetric directional coupler and for an asymmetric directional coupler. A combination of the EIM and the WKB normal mode approach is used to calculate the coupling length of a directional coupler with a graded-index profile. This semi-analytical

techniques involves the seperation of a 2-D differential equation into two 1-D differential equations. This allows us to perform the analysis rather easily using a small desktop computer.

In chapter 4, the graded-index waveguides are modelled to obtain the refractive index distribution profile for the quasi-TM mode. The modeling is divided into two cases, the finite diffusant source case and the infinite diffusant source case. A 2-D nonuniform FDM was developed for an efficient application of the boundary conditions.

In chapter 5, the conformal mapping technique is used for the analysis of various electrode structures including the coplanar strip (CS) and the complementary coplanar strip (CCS). Using this technique, the optimal positions of electrodes in relation to those of waveguides are determined. The developed mapping technique may be applicable to the electric field analysis even for the case of anisotropic material. The overlap integral between the optical field and the modulating RF field is calculated based on the results of the above field analysis.

In chapter 6, the coupled mode theory is used to analyze the behavior of a uniform directional coupler (DC), alternating $\Delta\beta$ DC, and a Y-branch DC in a precisely normalized form. It is shown that the coupling length of a Y-branch DC is 70% of that of a uniform DC for the same channel width and gap. Based on this fact, the coupling length of a Y-branch DC can be obtained when the coupling length of a uniform DC is calculated using the theories of Chapter 2, 3, and 4.

In chapter 7, the analysis of a traveling-wave electrode is implemented via a transmission line approach. Modulation depth is a function of many

factors, microwave frequency, source impedance, electrode impedance, load impedance, transit time difference between the optical and RF field, electrode conductive loss, and electrode length. Through the analysis of the modulation depth, the bandwidth of the traveling-wave device can be estimated.

In chapter 8, the detailed design procedure of a Y-branch directional coupler is presented, and the design of a traveling-wave electrode is illustrated. The design procedure is based on the theories of Chapter 2 to Chapter 7. The fabrication process of the $LiNbO_3$ optical modulator is described in detail.

In chapter 9, a block diagram of an optical measurement set-up to test switching operation of the Y-branch optical switch is presented. The output power of one branch as a function of a normalized voltage is shown. The length of the device, the switching voltages, the measured extinction ratios, and the estimated RF bandwidths are illustrated.

In our work, we have designed a Y-branch directional coupler optical modulator with a traveling-wave electrode to achieve the high-speed switching operation in Ti $LiNbO_3$. By employing the Y-branch directional coupler, we have reduced the device length by 30% in comparison with the conventional uniform directional coupler. This enabled us to achieve a device with a large bandwidth. We have also designed a traveling-wave electrode of semi-infinite coplanar strip structure in order to achieve high-speed operation.

The dc test showed that the coupling length of the Y-directional coupler is was about 3.25 cm. The switching voltage of the device was nearly ±2.5 V

and the extinction ratio was 17 dB. We have fabricated two samples with coupling lengths of l_y and 0.75 l_y. The switching voltage and extinction ratio of the device of 0.75 l_y were 28 V and 13 dB, respectively. Since we emphasized the large bandwidth, the device of 0.75 l_y was chosen for RF test at the cost of having a high switching voltage and a low extinction ratio. The projected bandwidth of the device is about 23 GHz. The microwave test will be conducted in the near future.

CHAPTER 2

EFFECTIVE INDEX METHOD (EIM) AND EVALUATION OF ERROR

Mathematical approaches to the mode dispersion in uniform rectangular waveguides have been attempted by extensive computer calculations such as the finite-difference method, the finite-element method, the variational method and so on. In 1969 Marcatili presented an approximate analysis of rectangular waveguides by assuming a simple field distribution [31]. In the same year, Goell provided a numerical solution for the propagation constant of rectangular waveguides by way of circular harmonic analysis [32]. Both the approximate analytical and numerical methods give reasonable and acceptable results. However, their applicability is limited to simple step-index rectangular waveguides.

In 1974, Knox and Toulios proposed the effective index method (EIM) which could be applied to any kind of structure [33]. This method is simple in its application but less accurate near the cut-off region. This method replaces the original Helmholtz 2-D differential equation with two 1-D equations. This allows estimation of approximate values of quantities such as the mode effective index and the propagation constant to be determined, thus eliminating the need for extensive computer calculations. This EIM involves considering a 1-D slab guide with respect to the y-direction as shown in Fig.2.1. The eigenvalue calculated in Fig.2.1b is now used to define the effective index of Fig.2.1c. The propagation constant of this second slab guide, shown in Fig.2.1c, represents the original rectangular

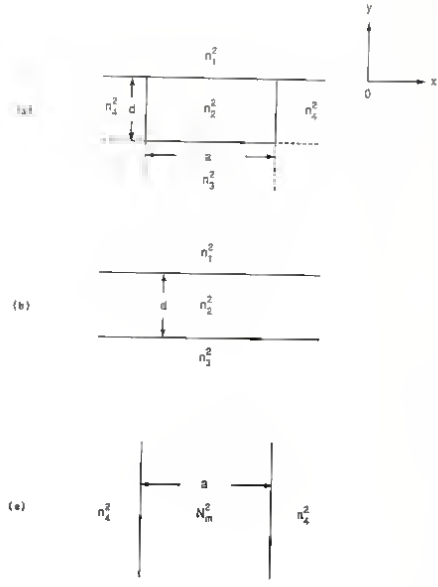

Fig 2.1 (a) Rectangular dielectric waveguide
(b)-(c) Substituted slab waveguides for the EIM

waveguide of Fig.2.1e. This approach gives somewhat closer results to the circular harmonic analysis of Goell than Marcatili's method for modes near cutoff. Although the error of the EIM is the vicinity of cut-off, especially for the fundamental mode and second-order mode, cannot be ignored the method has been widely used since it is simple, useful, and has acceptable error in most cases. The same technique has been extended to the optical strip-loaded waveguide [34]. The technique has also been very useful to device designers and others interested in diffused channel waveguides (16,35 36].

We will describe the EIM for a step-index waveguide and evaluate the particular error of the method. The scalar Helmholtz equation for the modal field is as follows

$$\nabla^2 E + \nabla(E\,\nabla\varepsilon^2/\varepsilon^2) + k^2\varepsilon^2 E = 0 \tag{2.1}$$

Since $\nabla\varepsilon^2 = 0$ in each medium of Fig.2.1e, the original wave equation reduces to

$$\frac{\partial^2}{\partial x^2} E(x,y) + \frac{\partial^2}{\partial y^2} E(x,y) + k_o^2[n^2(x,y) - N_{mo}^2)\, E(x,y) = 0 \tag{2.2}$$

where $\beta_{mo} = k_o N_{mo}$; k_o is the free space wave number and $n(x,y)$ is the refractive index distribution of a given waveguide. β_{mo} and N_{mo} are propagation constant and mode index (m-th in y-direction and n-th in x-direction), respectively.

The EIM essentially uses the method of separation of variables to solve the Helmholtz equation, assuming that the given index profile can be written as [37]

$$n^2(x,y) = n_1^2(y) + n_2^2(x) \tag{2.3}$$

If we write the dominant optical field as $E(x,y) = E_1(y)\, E_2(x)$,

$$\frac{E_1''(y)}{E_1(y)} + \frac{E_2''(x)}{E_2(x)} + k_o^2[\, n_1^2(y) + n_2^2(x) - N_{mn}^2] = 0 \tag{2.4}$$

where '' denotes second order differential with respect to the each direction. Consider first a 1-D slab guide with respect to the y-direction as shown in Fig.2.1b. The eigenvalue calculated in Fig.2.1b will be used to define an effective index of Fig.2.1c. Therefore, Eq.(2.4) can be rewritten as the following:

$$\frac{E_1''(y)}{E_1(y)} + \frac{E_2''(x)}{E_2(x)} + k_o^2[(n_1^2(y) - N_m^2) + (n_2^2(x) + N_m^2 - N_{mn}^2)] = 0 \tag{2.5}$$

By the method of separation of variables, Eq.(2.5) will be separated into two equations.

$$\frac{E_1''(y)}{E_1(y)} + k_o^2(n_1^2(y) - N_m^2) = 0 \tag{2.6}$$

$$\frac{E_2'(x)}{E_2(x)} + k_0^2[n_2^2(x) + N_m^2] - N_{mn}^2 = 0 \qquad (2.7)$$

where N_m is the m-th mode index of the slab waveguide of Fig.2.1b, the refractive index profile of which is

$$\begin{aligned} n_1^2(y) &= n_1^2 && y > 0 \\ &= n_2^2 && -d < y < 0 \\ &= n_3^2 && y < -d \end{aligned} \qquad (2.8)$$

Equation (2.7) shows that N_{mn} is the mode index of the n-th mode of a slab waveguide whose index distribution is given by $(n_2^2(x) + N_m^2)$. According to the EIM, the index distribution of Eq.(2.7) is equivalent to putting

$$\begin{aligned} n_2^2(x) + N_m^2 &= N_m^2 && 0 < x < a \\ &= n_4^2 && \text{elsewhere} \end{aligned} \qquad (2.9)$$

which means

$$\begin{aligned} n_2^2(x) &= 0 && 0 < x < a \\ &= n_4^2 - N_m^2 && \text{elsewhere} \end{aligned} \qquad (2.10)$$

By substituting Eq.(2.8) and (2.10) into Eq.(2.3), we have the index profile $n^2(x,y)$ of Fig.2.2, which is different from the actual index profile of Fig.2.1a. From Fig.2.2 of the EIM we see that $n^2(x,y)$ has a lower value in

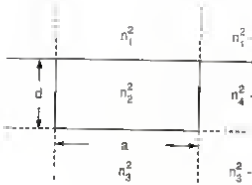

Fig 2.2 Dielectric constant distribution $n^2(x,y)$ described by Eqs (2.3), (2.8) and (2.10)

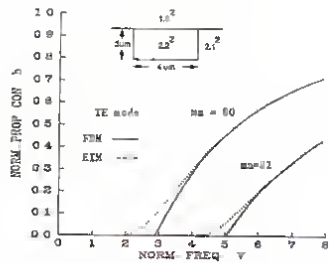

Fig 2.3 Comparison of results between the EIM and the 2-D FDM where $V = ka(n_2^2 - n_3^2)^{1/2}$, $b = (N_m^2 - n_3^2)/(n_2^2 - n_3^2)$

the corner region than in the original case of Fig 2.1a by the amount of $(N_m^2 - n_4^2)$. However, since the effect of the corner region is negligible, this index difference can be ignored. We also see that $n^2(x,y)$ has a higher value in the cladding region next to the core region than in the original case by the amount $(n_2^2 - N_m^2)$. This explains why the EIM gives higher values of the propagation constants for various guided modes than other rigorous solutions. When the field profile is highly confined, N_m approaches core index n_2, and the index area in the cladding region, $(n_2^2 - N_m^2)$, goes to zero. As a result the index profile (Fig 2.2) of EIM approaches the original index profile of Fig.2.1a and, therefore, the eigenvalues of EIM are almost exact. In the case of a weakly confined field profile, N_m approaches the index of a cladding layer with increasing index error. Thus, the index profile of EIM deviates from the actual index profile, resulting in increased error in the eigenvalues. The results of EIM are illustrated in Fig.2.3, where results of the finite difference method (FDM) are also shown for comparison. A modified EIM has been suggested that showed significant reduction of error near the cut-off [38].

CHAPTER 3

WKB ANALYSIS OF GUIDED-WAVE STRUCTURES

The phenomenon of coupled waves between two adjacent channels has been investigated extensively by a number of authors [39-42]. Analysis of the directional coupler can be carried out either by the normal mode approach of the overall coupler or by the coupled mode approach of the separate waveguides. Relationship between the normal mode and the coupled mode theory in case of weak coupling is already available [41]. For a strong coupling case, error in the coupled mode approach increases [43].

In this chapter, the eigenvalue equations for a symmetric coupler with graded-index profile are presented using the WKB approximation with the aid of Airy function. We assume each of the diffused waveguides comprising the coupled structure to have a Gaussian index profile in the depth direction and a composite error function index profile in the lateral direction. We analyze both a single channel waveguide and the symmetric directional coupler through a combination of the effective index method and the WKB method [16].

WKB Theory

In a planar waveguide with arbitrary index profile, the equation for the field distribution is

$$\frac{d^2}{dx^2}E(x) + V^2(E(x)-b)E(x) = 0 \qquad (3.1)$$

where V is an arbitrary constant, E(x) is an eigenfunction, and b is an eigenvalue to be determined. Equation (3.1) is the normalised 1-D scalar Helmoltz equation for the field distribution and is also the Shrodinger equation when $V^2[E(x)-b]$ is replaced by $(2m/h^2)[E-E(x)]$. Referring to Fig.3.1a, the approximate WKB solutions are given (44)

$$E(x) \sim c_1 P(x)^{-1/2} \exp\{ \int P(x)dx\} \qquad \text{for region I and III} \qquad (3.2a)$$

$$E(x) \sim c_2 Q(x)^{-1/2} \exp\{j\int Q(x)dx\} \qquad \text{for region II} \qquad (3.2b)$$

where $Q(x) = V^2(E(x)-b)$, $P(x) = V^2[b-E(X)]$.

The solution for region III will be of the same form as for region I. The accuracy of these WKB solutions can be guaranteed when the variation of dielectric permittivity is small over distances of the order of the wavelength. However at the turning point, the approximation fails because Eqs (3.2) diverge. The asymptotic solutions can be useful if we know how to connect two field solutions on each side of the turning point. Substituting $V^2(E(x)-b) \sim -s(x-x_2)$ around $x \sim x_2$ and performing the differentiation, we obtain

$$\frac{d^2E}{ds^2} - zE = 0 \qquad \text{where} \quad z = s^{1/3}(x-x_2) \qquad (3.3)$$

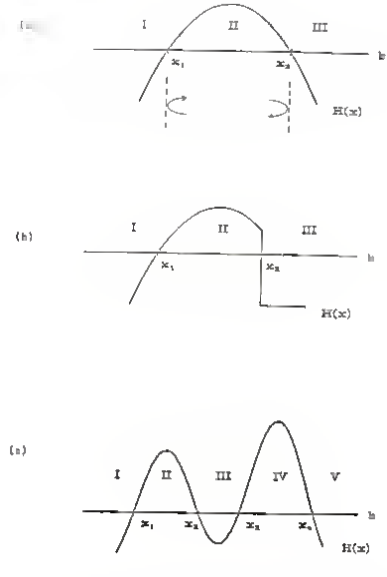

Fig-3 1 Index distribution and the turning points in (a) Graded-index channel waveguide (b) Graded-index guide with a discontinuity (c) Graded-index directional coupler

The same procedure can be carried out near $x \sim x_1$.

The solution of Eq.(3.3) is the Airy function. This function has two independent solutions, viz., Ai(z) and Bi(z). Both of them are continuous through the turning point $z \sim 0$. The asymptotic forms of the Airy functions [44,45] are given by

$$Ai(x) \sim e^{-\gamma}/(2\pi^{1/2}z^{1/4}) \tag{3.4a}$$

$$Ai(-z) \sim \sin(\gamma+\pi/4)/(\pi^{1/2}z^{1/4}) \tag{3.4b}$$

$$Bi(z) \sim e^{-\gamma}/(\pi^{1/2}z^{1/4}) \tag{3.4c}$$

$$Ai(z) \sim \cos(\gamma+\pi/4)/(\pi^{1/2}z^{1/4}) \tag{3.4d}$$

where $\gamma = \frac{2}{3} z^{3/2}$ and $z > 0$

Considering the continuity of the fields at the turning points and using Eqs (3.4), we find the independent connection formulae relating the fields on either side of the turning point.

For $x = x_1$ of Fig 3.1a,

$$p^{-1/2}\exp(-\int_x^{x_1} p\,dx) \longrightarrow 2q^{-1/2}\sin(\int_{x_1}^{x} q\,dx + \pi/4) \tag{3.5a}$$

$$p^{-1/2}\exp(\int_0^{x_1} p\,dx) \longrightarrow q^{-1/2}\cos(\int_{x_1}^{x} q\,dx + \pi/4) \tag{3.5b}$$

For $a = a_2$ of Fig 3.1a,

$$2Q^{-1/2}\sin\left(\int_a^{x_2} Q\,dx + \pi/4\right) \quad \text{——} \quad P^{-1/2}\exp\left(-\int_{a_2}^{a} P\,dx\right) \tag{3.6a}$$

$$Q^{-1/2}\cos\left(\int_a^{x_2} Q\,dx + \pi/4\right) \quad \text{——} \quad P^{-1/2}\exp\left(\int_{x_2}^{x} P\,dx\right) \tag{3.6b}$$

where the upper bound of the integral is always greater than the lower bound.

Two Turning Points (Single Channel Waveguide)

In the case of guided modes in a channel waveguide of Fig.3.1a, turning points occur at x_1 and a_2 with oscillatory behavior in the regions II and evanescent behavior elsewhere. Using the connection formulas, the solutions E(x) are

$$\text{I} \qquad P^{-1/2}\exp\left(-\int_a^{x_1} P\,dx\right) \tag{3.7a}$$

$$\text{II} \qquad 2Q^{-1/2}\left[\sin A \sin\left(\int_a^{x_2} Q\,dx + \pi/4\right) + \cos A \cos\left(\int_x^{a_2} Q\,dx + \pi/4\right)\right] \tag{3.7b}$$

$$\text{III} \qquad P^{-1/2}\sin A \exp\left(-\int_{x_2}^{x} P\,dx\right) + 2P^{-1/2}\cos A \exp\left(\int_{x_2}^{a} P\,dx\right) \tag{3.7c}$$

where $A = \int_{x_1}^{x_2} \beta dx = \int_{x_1}^{x_2} [H(x)-b]^{1/2} dx$

In the region III, the solution has to decay as $x \to \infty$ for the guided modes. Thus

$$V \int_{x_1}^{x_2} [H(x)-b]^{1/2} dx = (n + \frac{1}{2})\pi \qquad (3.8)$$

This eigenvalue equation can be applied to the analysis of a single optical waveguide with an arbitrary index profile. This equation can also be obtained by considering the total accumulation of the phase shift along the ray path and a phase shift of $\pi/2$ at the turning point [46].

Two Turning Points with an Index Discontinuity (Diffused Planar Waveguide)

When an index discontinuity occurs at $x = x_2$ shown in Fig.3.1b, as in a case of a diffused surface planar waveguide, the eigenvalue equation of Eq.(3.8) reduces to

$$V \int_{x_1}^{x_2} [H(x)-b]^{1/2} dx = (n + \frac{3}{4})\pi \qquad (3.9)$$

As before, the equation can again be obtained from the ray treatment of a mode in the waveguide with a phase shift of π at $x = x_2$ [46].

Four Turning Points (Directional Coupler)

In the case of a guided mode in a directional coupler of Fig.3 i.e. wave function is of oscillatory behavior in regions II and IV, and of evanescent behavior in regions I and V. In region III, wave function is a linear combination of exponentially decaying and growing waves. Using the connection formulae of Eqs.(3.5) and (3.6),

I, II and III same as Eq (3.7)

$$\text{IV}\quad Q^{-1/2}\sin A\exp(-B)\left[\cos C\sin\left(\int_{x}^{x_4} Q\,dx+\pi/4\right) - \sin C\cos\left(\int_{x}^{x_4} Q\,dx+\pi/4\right)\right]$$
$$+\ 4Q^{-1/2}\cos A\exp(B)\left[\sin C\sin\left(\int_{x}^{x_4} Q\,dx+\pi/4\right) + \cos C\cos\left(\int_{x}^{x_4} Q\,dx+\pi/4\right)\right] \qquad (3.10a)$$

$$\text{V:}\quad P^{-1/2}\sin A\exp(-B)\left[\tfrac{1}{2}\cos C\exp\left(-\int_{x_4}^{x} P\,dx\right) - \sin C\exp\left(\int_{x_4}^{x} P\,dx\right)\right]$$
$$+\ P^{-1/2}\cos A\exp(B)\left[2\sin C\exp\left(-\int_{x_4}^{x} P\,dx\right) + 4\cos C\exp\left(\int_{x_4}^{x} P\,dx\right)\right] \qquad (3.10b)$$

where $A = \int_{x_1}^{x_2} Q(x)\,dx$; $B = \int_{x_2}^{x_3} P(x)\,dx$, $C = \int_{x_3}^{x_4} Q(x)\,dx$

In region V, the solution has to decay as $x \to \infty$ for guided modes
Thus, we obtain

$$4\cos A\cos C\exp(B) - \sin A\sin C\exp(-B) = 0 \qquad (3.11a)$$

or, $\tan A \tan C = 4\exp(2B)$ (3.11b)

or, $(A + C) \pm \cos^{-1}[(\frac{1-\rho}{1+\rho})\cos(A - C)] = (2n + 1)\pi$ (3.11c)

where $\rho = \frac{1}{4}\exp(-2B)$

As seen from Eq. (3.11c), the modes are separated into quasi-even and quasi-odd modes. The plus and minus signs of denote the quasi-even and the quasi-odd modes respectively. In order to have the eigenvalue equations for both modes in the simplest form, we will use Eq. (3.11b).

1. Symmetric index profile

Since $A = C$ for symmetric profiles, Eq. (3.11b) can be easily reduced to

$$V\int_{x_1}^{x_2}[h(x)-b]^{1/2}dx \pm \tan^{-1}[\tfrac{1}{2}\exp(-V\int_{x_2}^{x_3}[h-h(x)]^{1/2}dx)] = (n + \tfrac{1}{2})\pi \qquad (3.12)$$

where the plus and minus signs denote the quasi-even and the quasi-odd modes, respectively. Under the condition stipulated by Eqs. (3.12) the field profile established in Eqs. (3.7) and (3.10) for the general case becomes symmetric or antisymmetric.

2. Asymmetric index profile

From Eq. (3.11b), we obtain the eigenvalue equations for the asymmetric coupled-structure with arbitrarily shaped index profiles.

$$V\int_{x_1}^{x_2}[H(x)-h]^{1/2}dx + \tan^{-1}\left[\frac{\tan\left(V\int_{x_3}^{x_4}[H(x)-h]^{1/2}dx\right)}{4\exp\left(2V\int_{x_2}^{x_3}(h-H(x)]^{1/2}dx\right)}\right] = (s+\frac{1}{2})\pi \qquad (3.13g)$$

$$V\int_{x_3}^{x_4}[H(x)-h]^{1/2}dx + \tan^{-1}\left[\frac{\tan\left(V\int_{x_1}^{x_2}(H(x)-h]^{1/2}dx\right)}{4\exp\left(2V\int_{x_2}^{x_3}[h-H(x)]^{1/2}dx\right)}\right] = (s+\frac{1}{2})\pi \qquad (3.13h)$$

Equations (3.13) constitute the quasi-even and quasi-odd mode eigenvalue equations. However, which of the two represents the even or odd mode cannot be predicted beforehand. That depends on the given index profile.

In summary, the differential equation (3.1) is converted to one of Eq. (3.8), Eq. (3.9), Eq. (3.12), and Eqs. (3.13) depending on the guiding structure.

Analysis of Graded-Index Channel Waveguides

Consider a channel waveguide formed by diffusion of a titanium strip of width w and thickness t (prior to the diffusion) as in Fig. 3.2a. The optimal index profile of the waveguide can be written as

$$n(x,y) = n_b + \Delta n \exp(-\eta^2)F(\xi,\delta) \qquad (3.14)$$

where $F(\xi,\delta) = \frac{1}{2}\{[\mathrm{erf}(\xi+\frac{\delta}{2}) - \mathrm{erf}(\xi-\frac{\delta}{2})]/\mathrm{erf}(\frac{\delta}{2})$, $\Delta n = n_s - n_b$, $\eta = y/d_y$, $\xi = x/d_x$, $\delta = w/d_x$, $d_y = 2(D_y t)^{1/2}$, $d_x = 2(D_x t)^{1/2}$

(a)

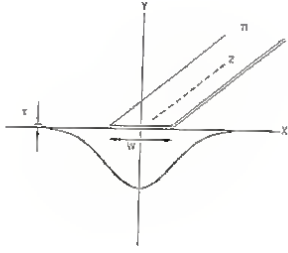

(b)

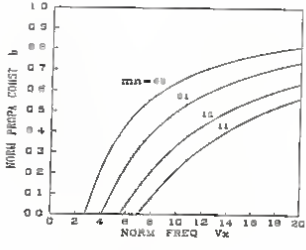

Fig.3 2 (a) Diffused channel waveguide. (b) b-V curve for the diffused waveguide with δ = 1 5

The variables d_x and d_y denote the diffusion lengths along the x and y axes, respectively while D_x and D_y represent the diffusion coefficients. The depth index profile is assumed to be Gaussian.

If we assume slowly inhomogeneity, i.e., $\lambda|\partial k/\partial x| \ll k$, Helmholtz equation of Eq. (2.1) also reduces to Eq. (2.2). Letting the dominant optical field $E_x(x,y) = E_1(y)E_2(x)$,

$$\frac{E_1''(y)}{E_1(y)} + \frac{E_2''(x)}{E_2(x)} + k^2[n^2(x,y) - N_e^2(x)] + k^2[N_e^2(x) - N_{me}^2] = 0 \qquad (3.15)$$

where $N_e(x)$ is a function of lateral effective index profile. The numbers, m and n, correspond to the mode number with respect to variation in the depth and lateral direction respectively. Equation (3.15) can be seperated into two 1-D differential equations by using the effective indexd method. The effective index essentially slices the 2-D graded index waveguide in the lateral direction. The mode index $N_e(x_o)$ corresponds to a given thin slice otd a specific value $x = x_o$. However the guide with an index profile $n(x_o,y)$ at $x = x_o$ is now assumed to be infinite in extent for the purpose of evaluating $N_e(x_o)$. $E_1(y)$ corresponding to that of $N_e(x)$ can be evaluated to obtain $E_2(x)$. Thus the application of the effective index method results in the following seperated equations.

$$\frac{d^2}{dy^2} E_1(y) + k^2[n^2(x,y) - N_e^2(x)]E_1(y) = 0 \qquad (3.16)$$

$$\frac{\delta^2}{dx^2} E_2(x) + k^2[N_e^2(x) - N_{mn}^2]E_2(x) = 0 \qquad (3.17)$$

In Eq. (3.16), since r is regarded as a constant, we can solve $N_e(x)$ at each point of x by applying the boundary condition along y — that is, along the depth direction. Equations (3.16) and (3.17) can be normalized after some algebraic manipulation:

$$[V_y^2 F(\xi,\delta)]^{-1}\frac{\delta^2}{d\eta^2} E_1(y) + [\exp(-\eta^2) - b_m(\xi,\delta,V_y)]E_1(y) = 0 \qquad (3.18)$$

$$V_m^{-2}\frac{d^2}{d\xi^2} E_2(x) + [F(\xi,\delta)b_m(\xi,\delta,V_y) - b_{mn}]E_2(x) = 0 \qquad (3.19)$$

where $V_x = k\delta_x(n_c^2-n_b^2)^{1/2}$, $V_y = k\delta_y(n_c^2-n_b^2)^{1/2}$, $F(\xi,\delta)b_m(\xi,\delta,V_y) = (N_e^2(x) - n_b^2)/(n_c^2 - n_b^2)$, and $b_{mn} = (N_{mn}^2 - n_b^2)/(n_c^2 - n_b^2)$. The variables V_x and V_y are the normalized frequencies in the x and y directions, respectively.

Note that Eq. (3.18) is for a diffused planar waveguide, and Eq. (3.19) is for a single channel waveguide. Therefore, by using Eqs. (3.9) and (3.5), Eqs. (3.18) and (3.19) reduce to the integral forms:

$$V_y F(\xi,\delta)^{1/2}\int_0^{\eta_t} [\exp(-\eta^2) - b_m(\xi,\delta,V_y)]^{1/2} d\eta = (m + \tfrac{3}{4})\pi \qquad (3.20)$$

$$V_x \int_{-\xi_t}^{\xi_t} [F(\xi,\delta)b_m(\xi,\delta,V_y) - b_{mn}]^{1/2} d\xi = (n + \tfrac{1}{2})\pi \qquad (3.21)$$

where η_t and ξ_t are the depth and lateral turning point, respectively. By solving Eq. (3.20) using a combination of the shooting method and the least square method bound by an accuracy of 10^{-3} we have [36]

$$b_m(\xi,\delta,V_y) = \sum_{r=1}^{4} a_r\{1 - (m\pi/4)(2\pi)^{1/2}/[V_y F(\xi,\delta)^{1/2}]\}^r \qquad (3.22)$$

where $a_1 = 0.09837$, $a_2 = 1.57489$, $a_3 = -1.12123$, $a_4 = 0.44296$. After substituting Eq. (3.22) into Eq. (3.21), Eq. (3.21) can then be solved by the shooting method for a certain set of δ, V_y and V_x. For the sake of simplicity we assume the diffusion to be isotropic and also uniform in the channel length. In Fig. 3.2b, dispersion curves are plotted for a typical strip width of $\delta = 1.5$, that is, $w/d_e = 1.5$, which is commonly encountered in titanium diffused $LiNbO_3$ channel waveguides. The dispersion curves vary on a small scale due to the change of strip width. For $\delta = 1.5$, the criterion for the waveguide to support a single mode is $2.69 < V_e < 4.04$.

Analysis of Symmetric Directional Coupler

A directional coupler with its identical, dual channel waveguides formed by diffusion of titanium strip of width w, and of separation s is shown in the Fig. 3.3a. The optical index profile of a directional coupler can be written as

$$n(\sigma,y) = n_b + \Delta n \exp(-\eta^2) G_e(\xi,\delta,\sigma) \qquad (3.23)$$

(a)

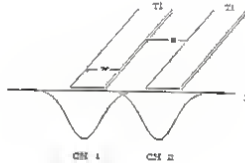

(b)

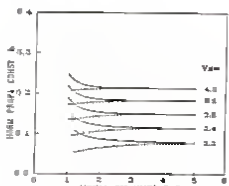

(c)

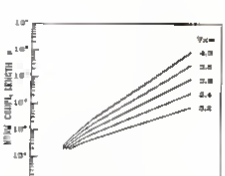

Fig 3.3 (a) Diffused symmetric directional coupler. (b) Normalized propagation constants vs. mode (solid) - odd mode (dotted) (c) Normalized coupling lengths vs. normalized channel gap

where $G_e(\xi,\delta,\sigma) = F(\xi + \frac{\delta}{2} + \frac{\sigma}{2}, \sigma) + F(\xi - \frac{\delta}{2} - \frac{\sigma}{2}, \sigma)$

$F(\xi,\delta) = \frac{1}{2}[\mathrm{erf}(\xi + \frac{\delta}{2}) - \mathrm{erf}(\xi - \frac{\delta}{2})]/\mathrm{erf}(\frac{\delta}{2})$, and $\sigma = s/d_x$.

With the same procedure between Eq.(3.14) and Eq.(3.19) we obtain

$$[V_y^2 G_e(\xi,\delta,\sigma)]^{-1}\frac{d^2}{d\eta^2} E_1(\eta) + [\exp(-\eta^2) - b_m(\xi,\delta,\sigma,V_y)]E_1(\eta) = 0 \qquad (3.24)$$

$$V_x^{-2}\frac{d^2}{d\xi^2} E_2(\alpha) + [G_e(\xi,\delta,\sigma)b_m(\xi,\delta,\sigma,V_y) - b_{mn}]E_2(\alpha) = 0 \qquad (3.25)$$

By use of Eq.(3.9) and (3.12), we get

$$V_y G_e(\xi,\delta,\sigma)^{1/2}\int_0^{\eta_t}[\exp(-\eta^2) - b_m(\xi,\delta,\sigma,V_y)]^{1/2}d\eta = (n + \tfrac{3}{4})\pi \qquad (3.26)$$

$$V_x\int_{\xi_1}^{\xi_2} Q(\xi,\delta,\sigma,V_y)d\xi \pm \tan^{-1}(\frac{1}{2}\exp(-V_x\int_{\xi_2}^{\xi_3} P(\xi,\delta,\sigma,V_y)d\xi)) = (n + \tfrac{1}{2})\pi \qquad (3.27)$$

where $Q(\xi,\delta,\sigma,V_y) = [G_e(\xi,\delta,\sigma)b_m(\xi,\delta,\sigma,V_y) - b_{mn(e,o)}]^{1/2}$

$P(\xi,\delta,\sigma,V_y) = [b_{mn(e,o)} - G_e(\xi,\delta,\sigma)b_m(\xi,\delta,\sigma,V_y)]^{1/2}$

and the plus and minus signs of Eq.(3.27) denotes the case of even(e) and odd(o) modes respectively. Solving Eq.(3.26) leads to

$$h_m(\xi,\delta,V_y) = \sum_{r=1}^{4} s_r[1 - (m+3/4)(2\pi)^{1/2}/[V_y G_e(\xi,\delta,\alpha)^{1/2}]]^r \qquad (3.28)$$

The coefficients s_r are the same as given in Eq.(3.22). Equation (3.28) is substituted in Eq.(3.27) and the resultant eigenvalue equation (3.27) is solved by way of the shooting method.

The coupling length of a symmetric, uniform directional coupler is written as one half of the beat period between even and odd mode.

$$l_c = \frac{\pi}{h}(N_{mne} - N_{mno})^{-1} = \frac{\lambda}{2}(N_{eme} - N_{mme})^{-1} \qquad (3.29)$$

which is approximated as

$$l_c = \frac{\lambda}{2\Delta n}(h_{mne} - h_{mno}) = \frac{\lambda}{2\Delta n}\mu \qquad (3.30)$$

where $\mu = (h_{mne} - h_{mno})^{-1}$ and is the normalized coupling length.

Note that coupling length varies linearly with μ. We assume the diffusion to be isotropic, i.e., $d_x = d_y$. In Fig.3.3b, eigenvalues of fundamental even and odd modes are plotted as a function of normalized channel gap ($s = s/d_y$). Normalized channel width δ is fixed at 1.5. In Fig.3.3c, the normalized coupling lengths are plotted for a range of normalized frequencies. When the gap between channels gets wider for a fixed V_y, overlapping of the evanescent field becomes weaker resulting in longer coupling lengths. From Fig.3.3c, it is seen that μ increases exponentially with the gap as expected from the viewpoint of the conventional coupled

mode theory. As V_a gets higher for a fixed value of σ, the evanescent field tail of such channel becomes weaker and a similar result is obtained.

CHAPTER 4

MODELING OF QUASI-TM GRADED-INDEX WAVEGUIDES

As the dielectric waveguide structures (e.g., graded-index waveguide and step-index waveguide including quantum well structures) become more diversified, the need for efficient computer analysis becomes greater and more demanding. A typical graded-index waveguide structure in $LiNbO_3$ and a simple step-index waveguide of GaAs are illustrated in Fig 4.1 In general the solutions to the Helmholtz equation for these structures are not easily amenable to exact analysis [47]

A number of numerical methods have been proposed to obtain rigorous solutions to the wave equation with pertinent boundary conditions Among the various computational methods, the finite difference method (FDM) has frequently been applied to various guided wave structures due to its simplicity [48-50]. One formalism of FDM utilizes the variational technique [48] and another scheme of FDM provides a solution of the wave equation directly in terms of the transverse component of the magnetic field [49]. Recently, semi-vectorial FDM with uniform discretization [50] has been introduced for the rib waveguide, where the waveguide is replaced by piecewise, continuous but constant refractive index. Finite element method has been also utilized to solve the wave equation by dividing the guided structure in arbitrary triangular forms [51-52]

In this work, first we extend the conventional FDM to include variable grid spacing in both directions facilitating the application of the

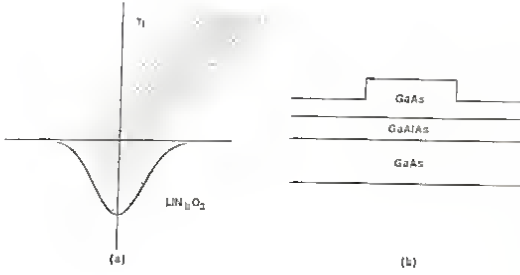

Fig 4.1 (a) $LiNbO_3$ channel waveguide, (b) GaAs waveguide

boundary conditions across abrupt index-changes for both quasi-TM and quasi-TE modes. This technique is flexible in that the method permits non-uniform discretization, which allows us to increase the size of the mesh far away from the guiding region, where the field vanishes. The grid spacing increases monotonically with increasing distance from the guiding region. The grid lines can also be aligned with the boundaries of the step index-changes in convectional structures such as rib, ridge and strip-loaded waveguides as well as custom cell structures. Secondly, through a judicial placement of the grid lines and corresponding cell structure, we can reduce the required memory size and hence the redundant computer calculations, while maintaining the desirable accuracy. The memory size is reduced to approximately one fourth of that of the conventional, uniformly spaced FDM, with similar accuracy, and therefore the amount of calculations as well as the computing time is considerably reduced. Obviously, increasing the number of grid lines increases the accuracy of the solutions.

We restrict our attention to the quasi-TM mode case since, for the same waveguide, the quasi-TM mode is much smaller in size and farther from the cutoff than the quasi-TM mode. This difference is attributed to the fact that ordinary index change $(\Delta n)_o$ is much smaller than extraordinary index change $(\Delta n)_e$ for x-cut Ti-diffused $LiNbO_3$ waveguides.

2-D Finite Difference Method (2-D FDM)

We assume that the fields are polarized perpendicular to the crystal surface and that the major field components of the modes are perpendicular

to the direction of the propagation (quasi-TM). Under the conditions of slowly varying inhomogeneity, wave equation for the dielectric waveguide with an arbitrary index profile is represented by

$$(\nabla_t^2 + k^2 n^2)E = \beta^2 E \qquad (4.1)$$

where ∇_t^2 is the transverse Laplacian and β is the propagation constant.

Figure 4.2a shows the grid lines used in the FDM formulation. The grid lines are placed in such a way that the spacing in the guiding region is rather small and increases gradually away from the waveguide. Boundaries of abrupt index-changes are straddled by the grid lines wherever necessary. A portion of the grid is re-drawn in Fig 4.2b for more detailed illustration. Each cell point is located in the center of each rectangle (cell). Each cell has sides of length h_i and h_j in horizontal and vertical directions, respectively. The refractive index within the cell is assumed to be uniform. Arbitrary spacing of the grid lines provides some flexibility in setting up the FDM. The non-uniform discretization with arbitrarily increasing spacing away from the guiding region permits the extention of the boundary (metal box in Fig.4.2), where the field are assumed to vanish.

Quasi-TM Mode

To apply the boundary conditions for the quasi-TM mode, we consider two adjacent cells (i,j) and (i,j+1) as shown in Fig.4.2b with the enlarged diagram in Fig.4.3. Note that the sequence of each cell's subscription (j)

(a)

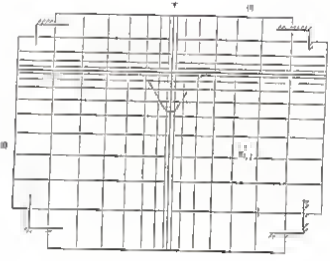

(b)

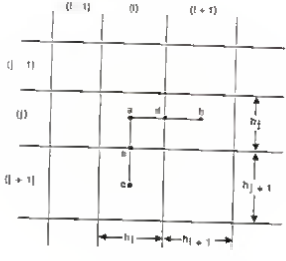

Fig.4.2 (a) Non-uniform grid lines for the FDM.
(b) Detailed sketch of a part of grid lines

mum increases with increasing y. $n_{i,j}$ and $n_{i,j+1}$ are selected to represent each cell of the continuous refractive index profile $n(o,y)$. The solid curves in Fig.4 3 indicate the actual profile of electric field amplitude. $E_{i,j}$ and $E_{i,j+1}$ are the field amplitudes representing each cell. E_n and E_s are the field amplitudes just to the north and south of the cell boundary. $E^{\bullet}_{i,j}$ and $E^{\bullet}_{i,j+1}$ are the virtual fields in the (i,j)th and (i,j+1)th cells, which are extensions of $E_{i,j+1}$ and $E_{i,j}$, respectively. n_n and n_s are the refractive index just to the north and south of the boundary. We again assume that n_n and n_s are approximately equal to $n_{i,j}$ and $n_{i,j+1}$, respectively. By applying the boundary condition along the boundary between two cells (i,j) and (i,j+1),

$$n^2_n E_n = n^2_s E_s \quad , \qquad \frac{\partial}{\partial y} E_n = \frac{\partial}{\partial y} E_s = q_+ \tag{4.2}$$

where q_+ is the field gradient at the boundary between the two cells. Equation (4.2) may be rewritten approximately as

$$n^2_{i,j} E_n = n^2_{i,j+1} E_s \quad , \qquad \frac{d}{\partial y} E_n = \frac{d}{\partial y} E_s = q_+ \tag{4.3}$$

Again, using the approximate relationship between $E_{i,j}$, $E_{i,j+1}$, $E^{\bullet}_{i,j}$, $E^{\bullet}_{i,j+1}$, we find

$$E_{i,j} \sim E_n + (h_j/2)\, q_+ \quad , \qquad E^{\bullet}_{i,j+1} \sim E_n - (h_{j+1}/2)\, q_+$$

$$E^{\bullet}_{i,j} \sim E_s + (h_j/2)\, q_+ \quad , \qquad E_{i,j+1} \sim E_s - (h_{j+1}/2)\, q_+ \tag{4.4}$$

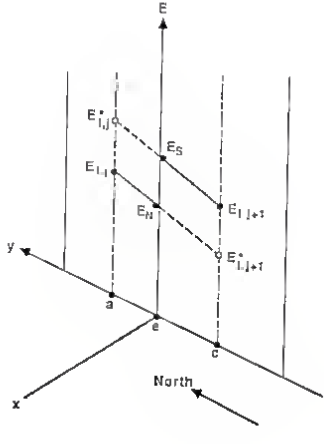

Fig 4-3 Field discontinuity at the boundary between cells (i,j) and (i,j+1)

where h_j and h_{j+i} are the vertical lengths of cells (i,j) and $(i,j+1)$. An algebraic manipulation of Eq.(4.4) renders

$$q_+ = 2(E_{i,j} - E^*_{i,j+1})/(h_j + h_{j+1}), \qquad E^*_{i,j+1} = E_{i,j+1} + (E_n - E_s)$$

$$h_{j+1}(E_{i,j} - E_o) = h_j(E_s - E^*_{i,j+1}), \qquad n^2_{i,j}E_n = n^2_{i,j+1}E_s \tag{4.5}$$

Substituting Eq.(4.5) into Eq.(4.3)

$$q_+ = 2(E_{i,j} - E^*_{i,j+1})/(h_j + h_{j+1}) \tag{4.6a}$$

$$E^*_{i,j+1} = \frac{n^2_{i,j+1}(h_j + h_{j+1})E_{i,j+1} + h_{j+1}(n^2_{i,j+1} - n^2_{i,j})E_{i,j}}{(n^2_{i,j}h_j + n^2_{i,j+1}h_{j+1})} \tag{4.6b}$$

Similarly, for the cell $(i,j-1)$ and (i,j), we obtain

$$q_- = 2(E^*_{i,j-1} - E_{i,j})/(h_{j-1} + h_j) \tag{4.7a}$$

$$E^*_{i,j-1} = \frac{n^2_{i,j-1}(h_j + h_{j-1})E_{i,j-1} + h_{j-1}(n^2_{i,j-1} - n^2_{i,j})E_{i,j}}{(n^2_{i,j}h_j + n^2_{i,j-1}h_{j-1})} \tag{4.7b}$$

where q_- is the field gradient at the boundary between cells $(i,j-1)$ and (i,j). As before, quasi-TM electric field is continuous along y-direction although refractive index is discontinuous. Therefore,

$$E^{*}_{i+1,j} = E_{i+1,j}, \quad E^{*}_{i-1,j} = E_{i-1,j} \tag{4.8}$$

Formulating the approximate second derivative,

$$\frac{\partial^2}{\partial x^2}E_{i,j} = \frac{1}{h_i}\left[\frac{2(E_{i+1,j} - E_{i,j})}{h_{i+1} + h_i} - \frac{2(E_{i,j} - E_{i-1,j})}{h_i + h_{i-1}}\right] \tag{4.9a}$$

$$\frac{\partial^2}{\partial y^2}E_{i,j} = \frac{1}{h_j}\left[\frac{2(E^{*}_{i,j-1} - E_{i,j})}{h_{j-1} + h_j} - \frac{2(E_{i,j} - E^{*}_{i,j+1})}{h_j + h_{j+1}}\right] \tag{4.9b}$$

Substituting Eq.(4.8) and (4.7) into Eq.(4.9)

$$\frac{\partial^2}{\partial x^2}E_{i,j} = \frac{1}{h_i}\left[\frac{2(E_{i+1,j} - E_{i,j})}{h_{i+1} + h_i} - \frac{2(E_{i,j} - E_{i-1,j})}{h_i + h_{i-1}}\right] \tag{4.10a}$$

$$\frac{\partial^2}{\partial y^2}E_{i,j} = \frac{2\,n^2_{i,j-1}}{h_j(n^2_{i,j}h_j + n^2_{i,j-1}h_{j-1})}E_{i,j-1} + \frac{2\,n^2_{i,j+1}}{h_j(n^2_{i,j}h_j + n^2_{i,j+1}h_{j+1})}E_{i,j+1}$$

$$- \left[\frac{2\,n^2_{i,j}}{h_j(n^2_{i,j}h_j + n^2_{i,j-1}h_{j-1})} + \frac{2\,n^2_{i,j}}{h_j(n^2_{i,j}h_j + n^2_{i,j+1}h_{j+1})}\right]E_{i,j} \tag{4.10b}$$

Eigenvalue Matrix [A]

The refractive index profile for a weakly guiding channel waveguide is given by

$$n(x,y) = n_b + \Delta n(x,y) \tag{4.11}$$

where n_b is the refractive index of the bulk (substrate) and $\Delta n(x,y)$ is the variation of the refractive index in the guiding region.

We assume that the grid is sliced into NY pieces along x-direction and NY pieces along y-direction. Equation (4.10) for the quasi-TM mode is substituted into Eq.(4-1). Each cell point yields a five-point linear equation in terms of $E_{i+1,j}$, $E_{i-1,j}$, $E_{i,j+1}$, $E_{i,j-1}$ and $E_{i,j}$. A set of linear equations for all the cell points (i = 1 ~ NX, j = 1 ~ NY) may now be rewritten in the following vectorial form.

$$[A][E] = \beta^2[E] \tag{4.12}$$

where the dimension of the matrix [A] is NX*NY by NX*NY. The matrix [A] is a real symmetric band matrix and the column vector [E] is the corresponding eigenvector representing the field $E(x,y)$. The vector element E_x, i.e., $E(x_i, y_j)$ in the column vector [E], is the field amplitude in the cell (i,j). The sequential arrangement of the field at each point is shown in Fig.4.4a. A typical structure of the matrix [A] of Eq.(4.12) is illustrated in Fig.4.4b, where the column vector [E] is represented by the set of elements

$$[E] = col(E_1, E_2, E_3, \ldots, E_x, \ldots, E_{NX*NY}) \tag{4.13}$$

where $x = (j-1)*NX + i$, and $i = 1,2,\ldots,NX$, $j = 1,2,\ldots,NY$)

(a)

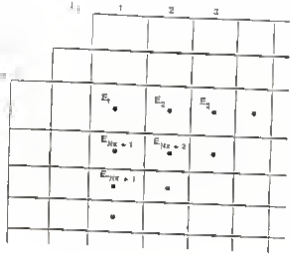

(b)

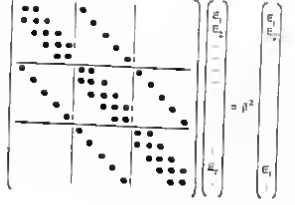

Fig.4.4 (a) Sequential arrangement of field points
(b) Illustration of a matrix with NX = 5 and NY = 3

The matrix [A] becomes the input data to the IMSL subroutine EIGRF to produce the eigenvectors [E] and the eigenvalue β. In this simulation, we use NX=22 and NY=17 with monotonically increasing spacing toward the metal box. The increase in spacing was chosen in a smooth but arbitrary fashion.

Modeling of Ti:$LiNbO_3$ Channel Waveguides

We apply this nonuniform FDM to model Ti diffused $LiNbO_3$ waveguides. In particular, we consider two cases: 1. finite source diffusion and 2. infinite source diffusion. In the case of diffusion time longer than that necessary to deplete the finite Ti source (finite source diffusion), index-distribution in the depth direction is Gaussian [53]. For the infinite source diffusion case, the complementary error function index profile is obtained in the depth direction [53]. Based on the above considerations, we model two cases:

1. small Ti thickness (700 A^o), finite source case.
2. large Ti thickness (1100 A^o), infinite source case.

Just-depleted case of intermediate thickness (900 A^o) is also discussed for the purpose of comparison.

It is well known that the termination of the diffusion process when the Ti (finite thickness) is just depleted results in Ti:$LiNbO_3$ waveguides with maximum index change at the surface. Optimization of the diffusion parameters and the channel width has resulted in minimum-mode-size waveguides [12] required for efficient overlap between the optical field and the modulating field. This allows us to fabricate high efficiency Ti:$LiNbO_3$

switches and modulators, with small voltage-length products. The single-mode-size waveguides with low-loss were fabricated by optimizing the fabrication parameters (Ti strip thickness of 800 Å and strip width of 4 μm, for 6 hours at 1025°C). For the quasi-TM mode, 1/e intensity full-width and full-depth were 3.9 μm and 2.8 μm respectively with low propagation loss (0.2 dB/cm) at 1.3 μm. Fabrication of such optical devices requires accurate knowledge of the refractive index profile, the diffusion lengths both in depth and lateral direction, and the surface refractive index change for the given set of fabrication parameters. Based on the knowledge above, we now estimate the electric field profiles of the waveguides and calculate the coupling-length of the directional couplers in terms of wavelength, guide dimension, peak index and channel gap.

Figure 4.5 shows the Ti:$LiNbO_3$ channel waveguide and the curved line indicates the graded-index profile in the lateral direction. In the figure, the propagation loss in terms of Ti strip width w was shown with the Ti strip thickness τ as a parameter [12]. We see that minimum propagation loss occurs when τ = 800 Å, which is the just-depleted case. Above 800 Å, we note that the propagation loss increases gradually with increasing thickness. The reason is that we still have a Ti residue on top of the crystal even after the diffusion. Below 800 Å, especially when the Ti strip width is narrow, Ti is fully diffused, resulting in weak guiding and close to the cut-off. As a result, mode sizes are considerably larger with decreasing Ti thickness. The propagation loss, therefore, becomes large as shown in the figure. As indicated previously, we consider the cases of τ = 700 Å (finite source), 800 Å (just depleted) and 1100 Å (infinite source)

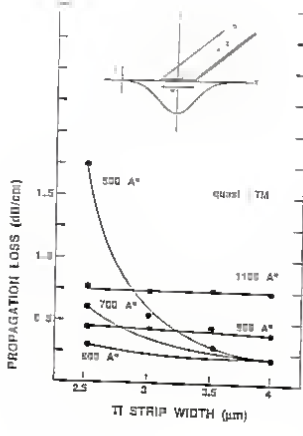

Fig.4.3 Quasi-TM propagation losses vs Ti width w with e parameter of Ti thickness t λ = 1.3 μm
(T = 1025 °C, t = 6 h)

for comparision between the experimental results and the theoretical simulation.

First, we consider the finite source case with the diffusion time longer than that required to just deplete the source.

i. Model 1 (diffusion time is longer than the exhaustion of Ti source)

The refractive index profile is described by an integration of Gaussian functions in the lateral direction, while the depth index profile is assumed to be a Gaussian function. This is true provided that the diffusant thickness is negligibly thin compared to the diffusion depth and that the diffusion time is long enough compared to that required to exhaust the Ti source [15-17].

$$\Delta n(x,y) = \frac{dn}{dc}\tau \int_{-w/2}^{w/2} \frac{2}{d\sqrt{\pi}} \exp[-(\frac{y}{d_y})^2] \frac{1}{d\sqrt{\pi}} \exp[-(\frac{\theta - x}{d_x})^2]\, d\theta \qquad (4.14)$$

$$= \Delta n_0 \exp[-(\frac{y}{d_y})^2] \frac{1}{2}[\mathrm{erf}(\frac{e + \frac{w}{2}}{d_x}) - \mathrm{erf}(\frac{x - \frac{w}{2}}{d_x})]/\mathrm{erf}(\frac{\frac{w}{2}}{d_x})$$

where $\Delta n_0 = \frac{dn}{dc}\frac{2}{\sqrt{\pi}}\frac{\tau}{d_y}\,\mathrm{erf}(\frac{\frac{w}{2}}{d_x})$, $d_x = 2(D_x t)^{1/2}$, $d_y = 2(D_y t)^{1/2}$,

c is the Ti concentration, and τ and w are the Ti strip thickness and width prior to the diffusion, respectively, as in Fig.4 5a.

2) Model 2) (diffusion time is shorter than the exhaustion of Ti source)

This model deals with the infinite source diffusant. The refractive index distribution for this case is given by an integration of the complimentary error functions in the lateral direction and the depth index profile is given by the complimentary function.

$$\Delta n(x,y) = \frac{dn}{dc} \tau \int_{-\theta/2}^{\theta/2} \frac{\sqrt{\pi}}{d_y} \operatorname{erfc}\left(\frac{|y|}{d_y}\right) \frac{\sqrt{\pi}}{2d_s} \operatorname{erfc}\left(\frac{|s-\theta|}{d_x}\right) ds \qquad (4.15)$$

$$= \Delta n_0 \operatorname{erfc}\left(\frac{|y|}{d_y}\right) \left[\left(\left(|s|+\frac{\theta}{2}\right)\operatorname{erfc}\left(\frac{|x|+\frac{\theta}{2}}{d_s}\right) + \left(\frac{\theta}{2}-|s|\right)\operatorname{erfc}\left(\frac{\frac{w}{2}-|x|}{d_s}\right)\right)\right.$$

$$\left. - \frac{d_s}{\sqrt{\pi}} \left\{\exp\left[-\left(\frac{|x|+\frac{\theta}{2}}{d_x}\right)^2\right] + \exp\left[-\left(\frac{\theta-|s|}{d_s}\right)^2\right]\right\} + \frac{2}{\sqrt{\pi}} d_x \right] / A_0 \qquad \text{for } |s| < \frac{w}{2}$$

$$= \Delta n_0 \operatorname{erfc}\left(\frac{|y|}{d_y}\right) \left[\left(\left(|s|+\frac{w}{2}\right)\operatorname{erfc}\left(\frac{|s|+\frac{w}{2}}{d_s}\right) - \left(|s|-\frac{\theta}{2}\right)\operatorname{erfc}\left(\frac{|s|-\frac{\theta}{2}}{d_x}\right)\right)\right.$$

$$\left. - \frac{d_s}{\sqrt{\pi}} \left\{\exp\left[-\left(\frac{|s|+\frac{\theta}{2}}{d_x}\right)^2\right] - \exp\left[-\left(\frac{|s|-\frac{\theta}{2}}{d_s}\right)^2\right]\right\} \right] / A_0 \qquad \text{for } |x| > \frac{w}{2}$$

where $\Delta n_0 = \frac{dn}{dc} \frac{\pi}{2} \frac{\tau}{d_y} \frac{A_0}{d_s}$, $A_0 = \theta \operatorname{erfc}\left(\frac{\theta}{2d_s}\right) + \frac{2d_x}{\sqrt{\pi}} \left(1 - \exp\left[-\left(\frac{\theta}{2d_s}\right)^2\right] \right)$

and Δn_0 is the surface index change after diffusion.

(a)

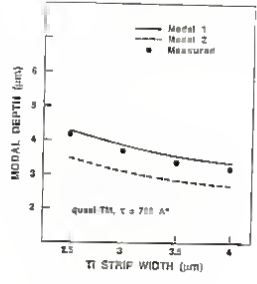

(b)

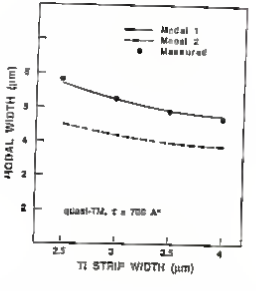

Fig 4-6 (a) Modal width, (b) Modal depth for τ = 700 A°

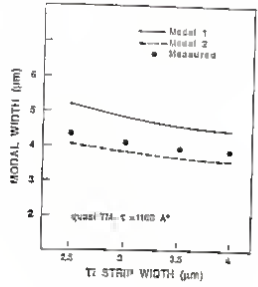

(b)

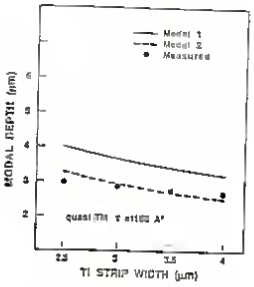

Fig 4.7 (a) Modal width (b) Modal depth for $\tau = 1100\ A^{0}$

(a)

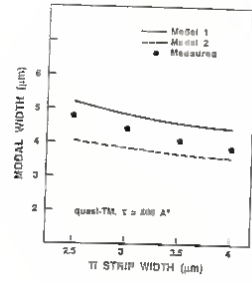

(b)

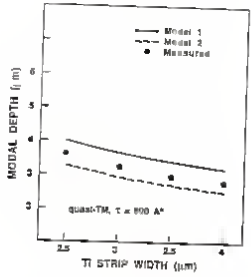

Fig 4-8 (a) Modal width, (b) Modal depth for τ = 800 A°

We calculate the quasi-TM mode sizes in both the lateral direction and the depth direction for Ti:LiNbO$_3$ waveguides with diffusion time equal to 6 hours at 1025°C. Ti thickness τ ranging 700 - 1100 Å, and Ti strip width ranging from 2.5 to 4 μm. We use both the models to fit the experimental results. The value dn/dx, for the extordinary axis, is assumed to be 0.625 [13,14,54]. Ti concentration c(x,y) is expressed as a fraction of that of pure Ti metal. d_x and d_y are calculated from the work of Ref.[15]. The measured values at 1025°C were such that $D_x = 1.2 \times 10^{-4}$ μm^2/sec and $D_y = 1.2 \times 10^{-4}$ μm^2/sec respectively. Therefore, $d_x = 3.2$ μm and $d_y = 3.2$ μm. Comparison of the calculated results with the experimental values is shown in Fig.4.6 through Fig.4.8 for τ = 700 Å, 1100 Å and 800 Å.

For the 700 Å of Fig.4.6, as expected, we note that the the model 1 of Gaussian index distribution fits very well with the experimental data. For 1100 Å as shown in Fig.4.7, the model 2 of complimentary error function distribution agrees well with the experimental data. In the case of 800 Å of Fig.4.8, we see the experimental results are between the model 1 and model 2. This is reasonable since the just deposited case is intermediate between the finite source case and the infinite source case.

CHAPTER 5

ELECTRODE ANALYSIS AND OVERLAP INTEGRAL FACTOR Γ

The efficiency of the modulator depends, in part, on the relative position of electrodes with respect to the waveguides. The case of infinite electrodes over an isotropic electrooptic material was presented by Marcuse [55]. It was shown that, for a push-pull directional coupler, the optimum spacing of the electrodes occurs when the inner edges of the electrodes are shifted towards the common center rather than directly above each of the optical waveguide center. The case of symmetric coplanar strip electrodes as well as the semi-infinite case were analysed by Ramer [56]. A rectangular dielectric waveguide in an isotropic substrate was assumed in his simulation.

In this chapter, we consider the problem of optimizing the electrode spacing and the relative position for the optical channel waveguides. The simulation is based on optimum, minimum mode size, split guided waveguides for single mode operation [12]. In the analysis of the modulating electric field we use a general conformal mapping function which handles asymmetric electrode structures as well as symmetric ones. The general field equations corresponding to the mapping function are derived and the functions are extended to the case of anisotropic substrates as well.

In the symmetric coplanar strip (CS) structure on z-cut $LiNbO_3$, it is shown that the maximum overlap integral Γ between the optical field and the modulating field occurs when the inner edge of the electrodes are aligned

with that of Ti-stripe prior to diffusion. Even if the relative positions are shifted a little bit from the optimum alignment, the overlap integral factor is not sensitively affected. In case that the electrode width is much larger than the Ti-strip width, as is often the case, the peak of the overlap integral factor is not significantly affected even if we vary the electrode width. The ratio of Γ to the gap between electrodes S is actually a more important parameter than Γ itself for modulator applications. It is also shown that, although Γ increases with increasing gap, the resultant peak value of the ratio Γ/S decreases. In the asymmetric CS, sum of two Γ factors remains essentially constant with varying degree of asymmetry; in other words, the sum remains almost the same even though one electrode width is larger or smaller than the other while the width of the other electrode remains constant.

Conformal Mapping Technique for Electrode Analysis

Figure 3.1 shows the placement of waveguides and electrodes. The electrodes are assumed to be infinitely thin compared to the width. One electrode is at zero potential while the other is at the potential V_0. Since the index change and hence the change in the dielectric constant due to Ti diffusion used in fabricating the waveguides is rather small, its effect is neglected in the analysis. The permittivity tensor is diagonal and the electrostatic potential $\phi(x,y)$ is a solution of the Laplace equation.

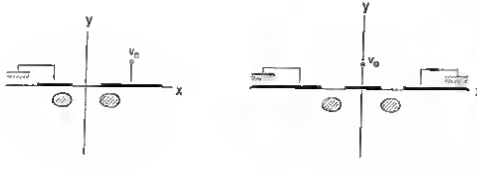

Fig 5.1 (a) Coplanar strip (CS) electrode
(b) Complementary coplanar strip (CCS) electrode

$$\varepsilon_x \frac{\partial^2 \phi}{\partial x^2} + \varepsilon_y \frac{\partial^2 \phi}{\partial y^2} = 0 \qquad \text{for } y < 0 \tag{5.1a}$$

$$\frac{\partial^2 \phi}{\partial x^2} + \frac{\partial^2 \phi}{\partial y^2} = 0 \qquad \text{for } y > 0 \tag{5.1b}$$

Equation (5.1a) can be rewritten as

$$\frac{\partial^2 \phi}{\partial x^2} + \frac{\partial^2 \phi}{\partial y'^2} = 0 \qquad \text{where } y' = (\varepsilon_x/\varepsilon_y)^{1/2} y \tag{5.2}$$

As seen from the Fig. 5.2, four-point representation a, b, c and d is versatile in that any two contiguous points can either represent an electrode or the gap between the electrodes. For the symmetric case, it is customary to solve the Laplace equation in the w-plane instead of the z-plane. For an arbitary width of the strip electrode shown in Fig.2, we can obtain the following general mapping function

$$z = \int_{x_1}^{x} \frac{[(x-c)(x-d)]^{1/2}}{(x-a)^{1/2}(x-b)^{1/2}(x-c)^{1/2}(x-d)^{1/2}} dx = \int_{x_1}^{z} \left(\frac{dw}{dz}\right) dz \tag{5.3}$$

where

$$z = x + jy' \,, \qquad w = u + jv \tag{5.4}$$

The lower bound of the integral x_1 can be any arbitrary point in the x-plane. Here, we put $x_1 = b$ for the sake of convenience. The mapping procedure from the original z-plane geometry into the w-plane [57-59] is

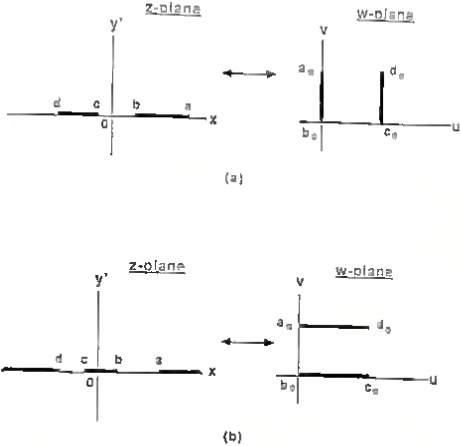

Fig-5-2 Conformal mapping for (a) CS electrode, (b) CCS electrode

shows in Fig.5.2. In the figure e_0, k_0, c_0, d_0 in the w-plane correspond to e,k,c,d in the x-plane respectively. It follows then,

$$\int_b^c \left(\frac{dw}{dx}\right) dx = 2F\left(\frac{\pi}{2}, k\right) = 2K(k) \tag{5.5a}$$

$$\int_c^d \left(\frac{dw}{dx}\right) dx = \int_k^e \left(\frac{dw}{dx}\right) dx = j2F\left(\frac{\pi}{2}, k'\right) = j2K(k') = j2K'(k) \tag{5.5b}$$

$$\int_{-\infty}^d \left(\frac{dw}{dx}\right) dx = \int_e^\infty \left(\frac{dw}{dx}\right) dx = F\left(\frac{\pi}{2}, k\right) = K(k) \tag{5.5c}$$

where

$$k = \left[\frac{(b-e)(c-d)}{(c-e)(b-d)}\right]^{1/2}, \quad k' = \left[\frac{(a-k)(c-d)}{(c-e)(k-d)}\right]^{1/2} \tag{5.6a}$$

$$k^2 + k'^2 = 1 \tag{5.6b}$$

$F(\theta,k)$ is the elliptic integral of first kind and $K(k)$ is the complete elliptic integral of $F(\theta,k)$ in the special case $\theta = \pi/2$. k is the modulus of the elliptic integral function and k' is its complementary modulus. Noting that $x_1 = k$ in Eq. (5.3), we have

$$e_0 = j2K(k) = j2K'(k) \tag{5.7a}$$

$$k_0 = 0 \tag{5.7b}$$

$$c_0 = 2K(k) \tag{5.7c}$$

$$d_0 = 2K(k) + j2K(k') = 2K(k) + j2K'(k) \tag{5.7d}$$

where K'(k) is the complementary function of K(k). From the w-plane of Fig.5.2, we have an approximate potential function $\phi(\sigma,v)$, with the corresponding capacitance C_0 per unit length and the characteristic impedance Z_0.

For coplanar strip (CS) electrodes,

$$\phi(\sigma,v) = V_0\left(1 - \frac{v}{|a_0|}\right) \tag{5.8a}$$

$$C_0 = \varepsilon_0\varepsilon_r \frac{|a_0|}{|a_0|} + \varepsilon_0 \frac{|a_0|}{|a_0|} = (2\varepsilon_0\varepsilon_{reff}) \frac{|a_0|}{|a_0|} \tag{5.8b}$$

$$Z_0 = \frac{1}{v_{ph} C_0} = \frac{1}{2}\left(\frac{\mu_0}{\varepsilon_0\varepsilon_{reff}}\right)^{1/2} \frac{|a_0|}{|a_0|} = 60\pi\,(\varepsilon_{reff})^{-1/2} \frac{|a_0|}{|a_0|} \tag{5.8c}$$

where $\varepsilon_r = (\varepsilon_x\varepsilon_y)^{1/2}$, $\varepsilon_{reff} = (\varepsilon_r + 1)/2$, $v_{ph} = (\varepsilon_0\mu_0)^{-1/2}(\varepsilon_{reff})^{-1/2}$

For complementary coplanar strip (CCS) electrodes,

$$\phi(\sigma,v) = V_0\left(1 - \frac{v}{|a_0|}\right) \tag{5.9a}$$

$$C_0 = \varepsilon_0\varepsilon_r \frac{|a_0|}{|a_0|} + \varepsilon_0 \frac{|a_0|}{|a_0|} = (2\varepsilon_0\varepsilon_{reff}) \frac{|a_0|}{|a_0|} \tag{5.9b}$$

$$Z_0 = \frac{1}{v_{ph} C_0} = \frac{1}{2}\left(\frac{\mu_0}{\varepsilon_0\varepsilon_{reff}}\right)^{1/2} \frac{|a_0|}{|a_0|} = 60\pi\,(\varepsilon_{reff})^{-1/2} \frac{|a_0|}{|a_0|} \tag{5.9c}$$

In Eqs (5.8a) and (5.9a), we assume that the potential ϕ varies linearly with u and v, respectively. One side of the electrodes gap in the w-plane of Fig.5.2 corresponds to the line between the electrodes in the z-plane. Along the side of the electrodes gap in the w-plane, the representation of ϕ is not accurate due to the fringing electric field. The contribution of the electric field around the surface of the z-plane to the overlap integral factor is almost negligible. Therefore, we ignore the fringing field effect in calculating Γ factor without the loss of generality. We are interested in solving the electric field in the substrate region, namely, $y < 0$ for calculating the overlap integral factor Γ between the electric and optical fields. Since we have the solution $\phi(u,v)$ in the w-plane, we need to derive the components of the electric field in the substrate region of the original z-plane from $\phi(u,v)$ of w-plane.

$$E = -\nabla\phi = -\mathbf{a}_x\frac{\partial\phi}{\partial x} - \mathbf{a}_y\frac{\partial\phi}{\partial y} = \mathbf{a}_x E_x + \mathbf{a}_y E_y \tag{5.10}$$

where

$$E_x = -\left(\frac{\partial\phi}{\partial u}\frac{\partial u}{\partial x} + \frac{\partial\phi}{\partial v}\frac{\partial v}{\partial x}\right) \tag{5.11a}$$

$$E_y = -\left(\frac{\partial\phi}{\partial u}\frac{\partial u}{\partial y} + \frac{\partial\phi}{\partial v}\frac{\partial v}{\partial y}\right) = -(\varepsilon_x/\varepsilon_y)^{1/2}\left(\frac{\partial\phi}{\partial u}\frac{\partial u}{\partial y'} + \frac{\partial\phi}{\partial v}\frac{\partial v}{\partial y'}\right) \tag{5.11b}$$

On the other hand,

$$dx + j\,dy' = \left[\mathrm{Re}\left(\frac{dz}{dw}\right) + j\,\mathrm{Im}\left(\frac{dz}{dw}\right)\right]du + j\left[\mathrm{Re}\left(\frac{dz}{dw}\right) + j\,\mathrm{Im}\left(\frac{dz}{dw}\right)\right]dv \tag{5.12}$$

Accordingly,

$$du + jdv = [Re(\frac{dw}{dz})dx - Im(\frac{dw}{dz})dy'] + j[Im(\frac{dw}{dz})dx + Re(\frac{dw}{dz})dy'] \qquad (5.13)$$

Applying Eq. (5.13) into Eqs. (5.11), we have

$$E_x = [-Re(\frac{dw}{dz})\frac{\partial \phi}{\partial u} - Im(\frac{dw}{dz})\frac{\partial \phi}{\partial v}] \qquad (5.14a)$$

$$E_y = (\varepsilon_x/\varepsilon_y)^{1/2}[Im(\frac{dw}{dz})\frac{\partial \phi}{\partial u} - Re(\frac{dw}{dz})\frac{\partial \phi}{\partial v}] \qquad (5.14b)$$

These equations are generally applicable as far as the conformal mapping techniques is concerned. We obtain the same results through Eq. (5.14) but in different form, if we now repeat the analysis by using $x' = (\varepsilon_y/\varepsilon_x)^{1/2}x$. Note that, in this case, the original electrodes' positions are differently scaled and the mapping function dw/dz will have a different form. Substituting Eqs. (5.8a) and (5.9a) into Eqs. (5.14), we obtain the following equations

For coplanar strip (CS) electrodes,

$$E_x = \frac{V_0}{|G_0|}\ Re(\frac{dw}{dz}) \qquad (5.15a)$$

$$E_y = -(\varepsilon_x/\varepsilon_y)^{1/2}\ \frac{V_0}{|G_0|}\ Im(\frac{dw}{dz}) \qquad (5.15b)$$

For complementary coplanar strip (CCS) electrodes,

$$E_x = \frac{V_0}{|\sigma_0|}\,\mathrm{Im}\left(\frac{dw}{dz}\right) \tag{5.16a}$$

$$E_y = \left(a_x/a_y\right)^{1/2}\frac{V_0}{|\sigma_0|}\,\mathrm{Re}\left(\frac{dw}{dz}\right) \tag{5.16b}$$

Semi-infinite electrodes and two-infinite electrodes are the special cases of the Fig.5.2 so that the general equations (5.3)-(5.7) are useful for any electrode structure. For instance, we can apply the conditions a+d=0, h+c=0 in case of the symmetric structure and the mapping functions are reduced to the well-known sine amplitude function. We also have square of sine amplitude function in case of semi-infinite electrodes and cosine hyperbolic function in two-infinite electrode case. Details of the derivation of these functions are shown in the Appendix A.

In Fig.5.3a, we show the electric field contours for the case of the symmetric CS structure. These field contours are plotted based on Eqs.(5.15) in conjunction with Eq.(5.3). As we see in the figures, field contours depend on the orientation of the crystal. The field contours of x-cut crystal are more oriented towards the depth-direction and those of x-set crystal are rather strongly directed along the lateral direction as compared to those for the isotropic case. That is because the dielectric constant for polarization along x-axis is smaller than the other. In Fig.5.3b, the asymmetric CS structure is dealt with. We recognize the same tendency of field orientation as in the symmetric case except that the field shape is no longer symmetric. In Fig.5.3c, field contours are drawn for the case of the symmetric CCS structure. Contours are obtained based on Eqs.(5.16) in

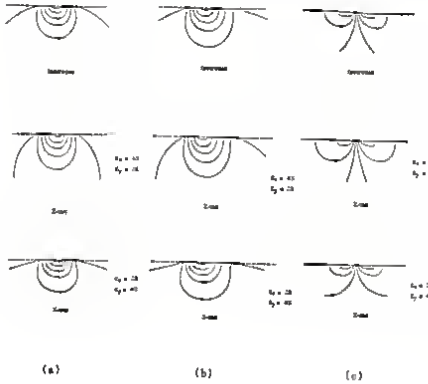

Fig 5.3 Electric field contours for (a) symmetric CS
(b) asymmetric CS, (c) symmetric CCS

conjunction with Eq (5.3). Field contours indicate a similar tendency as in the case of CS structure. In c-cut crystals, fields are more directed along the depth direction. In x-cut, these are more oriented towards the lateral direction.

In Fig 5.4, The amplitude of electric field components in symmetric CS structure are also plotted for z-cut $LiNbO_3$ substrate, where $\varepsilon_z = 43$ and $\varepsilon_y = 28$. The inner edge of one electrode is fixed at 2 μm and outer edge at 10 μm. The unique feature of these figures is the presence of a sharp peak near the edge of the electrode. As we shall see later this peak does not influence the overlap integral factor Γ significantly.

Overlap between RF field and Optical Field

To find the optimum placement of electrodes with respect to the position of channel waveguides, we need to know what the optical field profile will be. The change in the propagation constant $\Delta\beta$ of a guided mode due to a change in the extraordinary refractive index, in response to an externally applied voltage along the optical axis, is derived from a perturbation analysis

$$\Delta\beta \sim \frac{2\pi}{\lambda} \Delta n = \frac{2\pi}{\lambda} \left(\frac{1}{2} n^3 r_{33} \Gamma \frac{V_0}{S}\right) \tag{5.17}$$

where S is the gap between the electrodes and V_0 the applied voltage. The overlap integral factor Γ is defined as

(a)

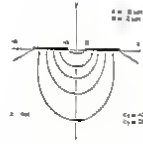

(b)

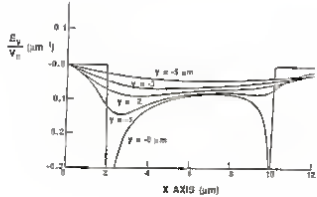

(c)

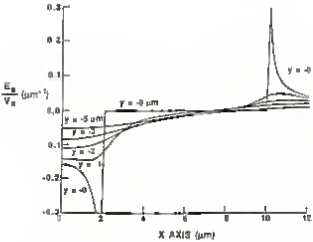

Fig 5 4 (a) Symmetric CS on z-cut $LiNbO_3$
(b),(c) Field amplitudes in y and x directions

$$\Gamma = \frac{S}{V_o} \frac{\iint E_{op}^2(x,y)\, E_{ol}(x,y)\, dxdy}{\iint E_{op}^2(x,y)\, dxdy} \qquad (5.16)$$

Γ equals Γ_1 if we deal with a single waveguide channel 1 only. When we consider the push-pull electro-optic effect on the channel waveguides for the general electrode structure, we need to evaluate Γ_1 and Γ_2 and the sum $\Gamma_1 + \Gamma_2$ represents Γ. The subscripts 1 and 2 denote the cases of the channel 1 and 2, respectively. Specifically, in case of symmetric electrode structures, Γ equals $2\Gamma_1$. E_{op} is the optical field and E_{el} the modulating electric field. When we consider a single channel waveguide 1, Γ_1 is to be calculated for the optical field profile $E_{op}(x,y)$ of channel waveguide 1 only. Note that, in case of the parallel electrode configuration like parallel capacitors, Γ_1 is unity since the electric field $E_{el}(x,y)$ is just a constant V_o/S independent of x and y.

Prior to evaluation of Γ, we need to know about the guided optical field profile $E_{op}(x,y)$. Field analysis for the diffused waveguides is easily simulated either by the effective index method or by the rigorous computational methods. However, it is well known that the fundamental mode field profile of the weakly guiding dielectric waveguides can approximately be represented by the Hermite-Gaussian function. Using this approximation for the transverse field profile in the optical waveguide located beneath the metal electrodes, we find

$$E_{op}^2(x,y) = \frac{4y^2}{w_x w_y^3 \pi} \exp[-(\frac{x-p}{w_x})^2] \exp[-(\frac{y}{w_y})^2] \qquad (5.17)$$

where p is the peak position of the optical field in the lateral direction. Note that the optical field is symmetric along the lateral direction. The widths of 1/e intensity of the above expression are $2w_x$ and $1.376w_y$ respectively

It has been reported [12] that ,for achieving minimum mode size, the diffusion of 4 μm wide and 800 Å thick Ti-strip was carried out for 6 hours at 1025 C. The experimental results showed that the quasi-TM mode had, in 1/e intensity, a width of 3.8 μm in the lateral direction and a width of 2.8 μm in the depth direction. For x-cut Ti-diffused $LiNbO_3$ waveguides, quasi-TM modes are well guided and the mode sizes are much smaller than those of quasi-TE modes. This difference is due to the fact that the extraordinary index change $(\Delta n)_e$ is much larger than the ordinary index change $(\Delta n)_o$. Throughout this work, we will use the above data for the mode profile $E_{ep}^2(x,y)$. Therefore, we use $w_x = w_y \sim 2$ μm in the simulations. Since Eq.(5.19) is already normalized to unity its direct substitution in Eq.(5.18) results in the overlap integral factor

$$\Gamma = \frac{S}{V_0} \frac{4}{w_x w_y^2 \pi} \iint y^2 \exp[-(\frac{x-p}{w_x})^2] \exp[-(\frac{y}{w_y})^2] E_{ei}(x,y)\, dxdy \qquad (5.28)$$

Figure 5.5e shows the case of symmetric CS electrodes on x-cut $LiNbO_3$ substrate. Figs.5.5h shows the overlap integral factor Γ_1 for the single waveguide as a function of the variable p (peak position of the optical field in the lateral direction) with parameters s and h (the electrode edge positions), respectively. As seen from [7], for typical directional

(a)

(b)

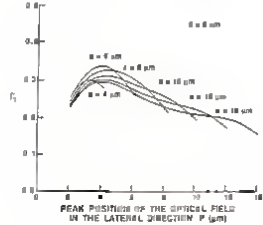

(c)

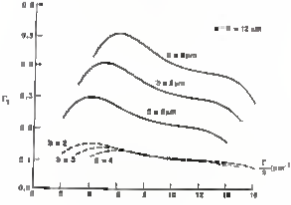

Fig.5.5 (a) Symmetric CS in x-cut $LiNbO_3$
(b)-(c) Overlap integral factors Γ_1

couplers, gap between the Ti stripe ranges from 4 μm to 6 μm. Therefore, in Fig.5.5b, point b is fixed at 2 μm so that the electrode gap is 4 μm and point a is varied from 4 μm to 14 μm. As seen from the figure, in general, the peak of Γ_1 always occurs away from the center of the electrode towards its inner edge. Γ_1 has a maximum value always around $y = 4$ μm. Exception to this case is when $a = 4$ μm, which is not actually useful since narrow electrodes is width result in high resistance and high impedance. The very interesting feature of Fig.5.5b is that the maximum value of Γ_1 occurs when the point of 1/e intensity edge of the optical power, namely, $x = (y - w_x)$ is near the inner electrode edge b. In other words, we have the maximum Γ_1 when the electrode inner edge falls on the Ti inner edge prior to diffusion, although this maximum is rather broad and shows only a slight advantage over other placements of the electrodes. In Fig.5.5c, we fix the width of the electrode as 12 μm, while varying the electrode gap. The maximum Γ_1 in both cases still occurs at a point so that 1/e intensity edge of the optical power is near the electrode edge. Here, we see several curves of Γ_1 dependency on the position of point b. However, we note that Γ/S should rather be the standard of comparison, instead of Γ itself since the electric field which influences the change in the optical propagation constant is inversely dependent on $\Gamma \frac{V}{S}$. We show the curves of Γ_1/S in the bottom of the figure for comparison.

In Fig.5.6, we show the asymmetric CS electrodes on a z-cut $LiNbO_3$ substrate, the variation of Γ_1, Γ_2, and Γ ($= \Gamma_1 + \Gamma_2$). In the calculation, we use $d = -10$ μm, $c = -2$ μm, $b = 2$ μm so that the width of the left-side electrode equals 8 μm and $y = 4$ μm as this is the maximum point of overlap

(a)

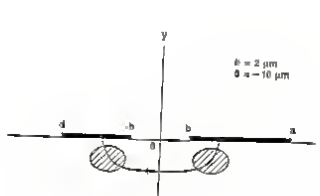

(b)

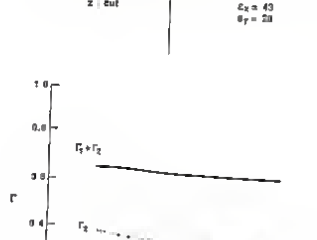

Fig.5.6 (a) Asymmetric CS on z-cut $LiNbO_3$
(b) Overlap integral factor Γ_1, Γ_2, and $\Gamma_1+\Gamma_1$

integral in the symmetric case as seen from Fig.5.5b. We change the width of the right-side electrode, while keeping the electrode gap constant. The wider the electrode is, the weaker the modulating field beneath the electrode becomes and the narrower the electrode is, the stronger the modulating field becomes. This is the reason why the overlap integral factors Γ_1 and Γ_2 present a push-pull effect with the variation of the outer edge point **a**. The overall overlap integral factor Γ gets slightly larger as the value of the outer edge of the electrode becomes smaller, which is actually not important because such a narrow width is not appropriate when considering the resistance and impedance of the electrodes. Even if the electric field intensity at the edge approaches infinity as shown in Fig.5.4, the edge field effect on Γ is almost negligible since the optical power goes to zero at an exponential rate. However, as seen from Fig.5.6, it is clear that Γ is insensitive to the degree of asymmetry of electrode width as long as the electrode width extends far beyond the optical mode field.

CHAPTER 6

COUPLED MODE THEORY FOR Y-BRANCH DIRECTIONAL COUPLER

Optical directional couplers usually consist of two waveguides placed parallel so that the fields of the fundamental modes in both waveguides overlap weakly. The presence of one waveguide now presents a small perturbation to the other and the power is exchanged between the transverse modes E1(x,y) and E2(x,y), where the numbers 1 and 2 denote each waveguide. In the case of this weak perturbation the propagating fields can be represented in complex notation (40),

$$E1(x,y,z,t) = A(z)E1(x,y)\exp[j(\omega t - \beta_1 z)] \tag{6.1a}$$

$$E2(x,y,z,t) = B(z)E2(x,y)\exp[j(\omega t - \beta_2 z)] \tag{6.1b}$$

where A(z) and B(z) are the normalized mode amplitudes of the electric fields in guides 1 and 2, respectively, and β is the propagation constant of the mode. The mode amplitudes A(z) and B(z) in each waveguide in this case are no longer constant but vary along z. As shown in Appendix B A(z) and B(z) obey the following coupled mode equations:

$$dA/dz = -jk_{12}\exp(-j2\delta z)B \tag{6.2a}$$

$$dB/dz = -jk_{21}\exp(j2\delta z)A \tag{6.2b}$$

where $\delta = (\beta_2 - \beta_1)/2 = A\beta/2$, $k = k_{12} \sim k_{21}$, $k^2 + \delta^2 = \kappa^2$ (6.2a)

and k is the coupling coefficient. Using substitution [60] of,

$$A = R \exp(-j\delta z) \quad , \qquad B = S \exp(j\delta z) \tag{6.3}$$

Equations (6.2) are transformed to

$$dR/dz - j\delta R = -jkS \tag{6.4a}$$

$$dS/dz + j\delta S = -jkR \tag{6.4b}$$

Note that $RR^* = AA^*$ and $SS^* = BB^*$. For arbitrary input amplitudes R_o and S_o, general solutions of Eqs (6.4) are

$$\begin{bmatrix} R \\ S \end{bmatrix} = \begin{bmatrix} \cosh'z + j\frac{\delta}{\kappa'}\sinh' z & -j\frac{k}{\kappa'}\sinh'z \\ -j\frac{k}{\kappa'}\sinh'z & \cosh'z - j\frac{\delta}{\kappa'}\sinh'z \end{bmatrix} \begin{bmatrix} R_o \\ S_o \end{bmatrix} \tag{6.5}$$

Note that the matrix's determinant is unity.

Uniform Directional Coupler

The schematic diagram of a uniform directional coupler is shown in Fig.6.1a. Let's assume that we launch the light at the input of S. For $R_o = 0$, $S_o = 1$,

$$R(z)R^*(z) = (k/\kappa')^2 \sin^2\kappa' z \ , \qquad S(z)S^*(z) = 1 - R(z)R^*(z) \tag{6.6}$$

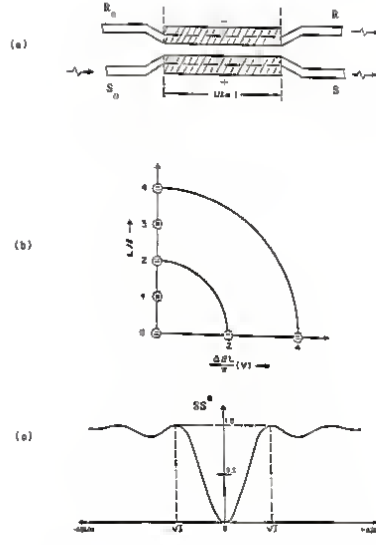

Fig 5.1 (a) Uniform directional coupler, (b) Switching diagram
(c) Power output SS^* for $L = L_0$

Complete power transfer occurs when

$$h' = h \quad (\delta = 0) \qquad \text{at} \quad z = z_c = \frac{\pi}{2k} \quad (k = \pi/2z_c) \tag{6.7}$$

z_c is the coupling length of a symmetric uniform directional coupler.

We introduce the variables such as

$$x = (\Delta\beta)L/\pi \quad , \quad y = L/z_c \quad \text{and} \quad r^2 = x^2 + y^2 \tag{6.8}$$

y and x are called the normalized coupling length and the normalized voltage, respectively. We have, then,

$$h = \pi/2z_c = (L/z_c)(\pi/2L) = y(\pi/2L) \tag{6.9}$$
$$\delta = \Delta\beta/2 = (\Delta\beta L/2)(\pi/2L) = x(\pi/2L) \quad \text{and} \quad h' = r(\pi/2L)$$

where L is the actual interaction length of the coupler.

Equation (6.5) then can be converted to the normalized matrix form.

When z = L (interaction length)

$$\begin{bmatrix} R \\ S \end{bmatrix} = [M] \begin{bmatrix} R_0 \\ S_0 \end{bmatrix} = \begin{bmatrix} a & b \\ h & a^* \end{bmatrix} \begin{bmatrix} R_0 \\ S_0 \end{bmatrix} \tag{6.10}$$

where [M] is called a transfer matrix and

$$a = \cos(\tfrac{\pi}{2}x) + j\tfrac{x}{r}\sin(\tfrac{\pi}{2}x) \quad , \quad b = -j\tfrac{y}{r}\sin(\tfrac{\pi}{2}x)$$

For $R_o = 0$; $S_o = 1$ $(z = L)$,

$$RR^* = bb^* = (y/z)^2 \sin^2(\frac{\pi}{2}z) \tag{6.11a}$$

$$SS^* = aa^* = 1 - bb^* = 1 - (y/z)^2 \sin^2(\frac{\pi}{2}z) \tag{6.11b}$$

To simplify the discussion, we denote the switching state where the light crosses over completely from one guide to the other as 's', the cross state. We also call the state in which the light appears in the same guide at the output as '=', the bar state. From Eqs.(6.9), we see the switching condition as

$$\text{'x'} \;:\; |b| = 1 \tag{6.12a}$$

$$\text{'='} \;:\; |b| = 0 \tag{6.12b}$$

In other words,

$$\text{'x'} \quad x = 0, \;\; z = y \;\; \text{and} \;\; z = 2N + 1 \quad (N = 0,1,2,\ldots) \tag{6.13a}$$

$$\text{'='} \quad x^2 + y^2 = z^2 \quad \text{and} \quad z = 2N \quad (N = 1,2,3,\ldots) \tag{6.13b}$$

The switching diagram is drawn in Fig.6.1b. From the figure, we notice that the state of $y = 1$ is the optimum condition for traveling back and forth between the 's' state and '=' state.

For $y = 1$ $(L = 1_o)$, the power output SS^* is, from Eq.(6.11b),

$$SS^* = 1 - \frac{1}{x^2+1}\sin^2\left[\frac{\pi}{2}(x^2+1)^{1/2}\right] \qquad (6.14)$$

SS^* is plotted as a function of normalized applied voltage x with a parameter of y in Fig. 6.1c.

Alternating $\Delta\beta$ Directional Coupler

Figure 6.2a shows a sketch of an alternating $\Delta\beta$ directional coupler configuration. In the figure, the interaction length L is devided into two equally long sections of L/2. We have $+\Delta\beta$ in the left section and $-\Delta\beta$ in the right section. We call the transfer matrix of the $+\Delta\beta$ section as $[M^+]$ and that of the $-\Delta\beta$ as $[M^-]$. Then $[M^+]$ and $[M^-]$ have the forms of

$$[M^+] = \begin{bmatrix} a_1 & b_1 \\ b_1 & a_1^* \end{bmatrix}, \qquad [M^-] = \begin{bmatrix} a_1^* & b_1 \\ b_1 & a_1 \end{bmatrix} \qquad (6.15)$$

where $a_1 = \cos(\frac{\pi}{4}x) + j\frac{x}{x}\sin(\frac{\pi}{4}x)$, $b_1 = -j\frac{y}{x}\sin(\frac{\pi}{4}x)$

The overall transfer matrix $[M]$ is obtained by matrix multiplication

$$\begin{bmatrix} R \\ S \end{bmatrix} = [M]\begin{bmatrix} R_o \\ S_o \end{bmatrix} = [M^+][M^-]\begin{bmatrix} R_o \\ S_o \end{bmatrix} = \begin{bmatrix} a_1a_1^* + b_1b_1 & 2a_1b_1 \\ 2a_1^*b_1 & a_1a_1^* + b_1b_1 \end{bmatrix}\begin{bmatrix} R_o \\ S_o \end{bmatrix} \qquad (6.16)$$

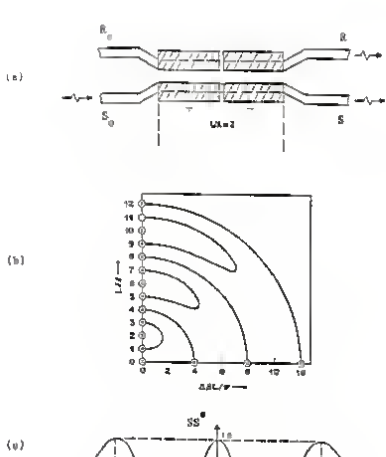

Fig 6.2 (a) Alternating Δβ directional coupler, (b) Switching diagram (c) Power output SS^* for $L = 2l_c$

For $R_0 = 0$, $S_0 = 1$

$$RR^* = 4|a_1|^2|b_1|^2 \tag{6.17a}$$

$$SS^* = (|a_1|^2 - |b_1|^2)^2 = (1 - 2|b_1^2|)^2 \tag{6.17b}$$

From Eqs.(6.17), we have the switching condition as

'o' $|b_1| = 1/\sqrt{2}$, '=' $|a_1| = 0$ or $|b_1| = 0$ (6.18)

Describing the above conditions in more detail,

'o' $(y/x)^2 \sin^2(\frac{\pi}{4}x) \approx \frac{1}{2}$ (6.19a)

'=' $x = 0$ and $x = 2(2N+1)$ $(N = 0,1,2,\ldots)$ (6.19b)

or $x^2 + y^2 = r^2$ and $x = 4N$ $(N = 0,1,2,\ldots)$

The switching diagram is sketched in Fig.6.2b. From the figure, we see that we have many options in selecting y $(= L/i_0)$. If we select $y = 1$, then we need to travel a long way back and forth between 'o' state $(\alpha = \pi)$ and '=' state, which means that we have to apply high voltage to effect a large $\Delta\beta$. The choice of $y = 2$ is preferable since we do not need to travel long way between two states. Note that, in this case, the interaction length of a device is doubled, that is, $L = 2I_0$.

For this $y = 2$, the power output $S3^*$ is then, from Eq.(6.17b),

$$SS^* = \left[1 - 2\frac{4}{x^2+4}\sin^2\left(\frac{\pi}{4}(x^2+4)^{1/2}\right)\right]^2 \qquad (6\ 20)$$

SS^* is plotted in Fig. 6.2a.

Y-Branch Directional Coupler

The Y-branch directional coupler is illustrated in Fig. 6.3a. Assuming that the coupling section of a Y-branch directional coupler has exactly the same geometry as that of the uniform directional coupler, the launched power will be divided evenly due to the symmetry of the coupling section. For $R_o = S_o = 1/\sqrt{2}$, Eqs. (6.10) reduce to

$$RR^* = \frac{1}{2}\left[1 - (2xy/r^2)\sin^2\left(\frac{\pi}{2}r\right)\right] \qquad (6\ 21a)$$

$$SS^* = \frac{1}{2}\left[1 + (2xy/r^2)\sin^2\left(\frac{\pi}{2}r\right)\right] \qquad (6\ 21b)$$

where $x = (A\beta/\pi)L$, $y = L/i_c$, $r^2 = x^2 + y^2$.

Complete power transfer first occurs when $x = y = 1/\sqrt{2}$ (or when $\delta = \pi/2i_c = h$, $h' = \sqrt{2}h$). This can be expressed as

$$RR^* = 0 \qquad \text{at} \quad L = l_y = \frac{i_c}{2\sqrt{2}h} = l_c/\sqrt{2} \qquad (6\ 22)$$

We note that i_y is shorter than l_c by a factor of $1/\sqrt{2}$.

This important result of a Y-branch directional coupler is one of the features in achieving a high-speed and a large bandwidth.

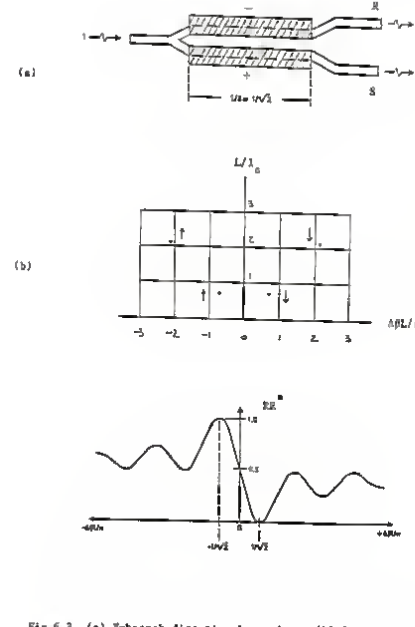

Fig 6.3 (a) Y-branch directional coupler. (b) Switching diagram (c) Power output P_R for $L = l_y$ ($= l_0/\sqrt{2}$)

In a Y-branch directional coupler, we have two kinds of cross states since there is only one input. We can define two states such that the '+' state is the case when the total power comes out of the upper section and that '-' state is the case when the total power comes out of the lower section.

From Eqs.(6.21),

$$'+' \quad : \quad -x = y = \pi/\sqrt{2} \quad \text{and} \quad x = 2N + 1 \qquad (N = 0,1,2,\ldots) \qquad (6.23a)$$

$$'-' \quad : \quad x = y = \pi/\sqrt{2} \quad \text{and} \quad x = 2N + 1 \qquad (N = 0,1,2,\ldots) \qquad (6.23b)$$

The switching diagram is illustrated in Fig.6.3b. As seen from the figure, when $y = 1/\sqrt{2}$, we not only have the shortest coupling length but also have the lowest applied voltage. Note that, in this case,

$$L = l_y = l_c/\sqrt{2} \ , \qquad A\beta = \pi/(\sqrt{2}l_y) = \pi/l_z \qquad (6.24)$$

For this $y = 1/\sqrt{2}$, the power output RR^* is, from Eq.(6.21a),

$$RR^* = \frac{1}{2}\left[1 - \frac{2x}{x^2 + \frac{1}{2}} \sin^2\left(\frac{\pi}{2}(x^2 + \frac{1}{2})^{1/2}\right)\right] \qquad (6.25)$$

The power output is plotted in Fig.6.3c.

As defined previously, $\Delta\beta$ is the difference of the propagation constants between the two channels of the directional coupler. On the other hand, using Eq.(5.17),

$$\Delta\beta = \frac{\pi}{l_\pi} = \frac{\pi}{2l_y} = \frac{2\pi}{\lambda}\left(\frac{1}{2}n^3 r_{33}\Gamma_t V_{sw}/S\right) \tag{6.26}$$

Γ_t is the sum of the two overlap integrals, which are due to the push-pull field effect on the two channel waveguides. Therefore, from Eq.(6.26),

$$V_{sw} = (\lambda S)/(n^3 r_{33}\Gamma_t l_\pi) = (\lambda S)/(\sqrt{2}n^3 r_{33}\Gamma_t l_y) \tag{6.27}$$

The switching voltage is inversely proportional to the coupling length.

CHAPTER 7

TRAVELING-WAVE ELECTRODE AND MODULATION DEPTH

The aim of using traveling-wave electrode is to achieve a high-speed optical modulator with a large bandwidth [4,5,10,19-22]. The bandwidth of the traveling-wave electrode is not limited by RC constant as in the lumped-type (standing-wave) electrode. Ideally, the RF traveling-wave will propagate at the same speed as the optical beam propagating under the electrode. This RF signal induces an electric field across the optical channel waveguides and, therefore, changes the extraordinary refractive index of the x-cut substrate. The change in the propagation constant of the guided mode due to the electro-optic effect, $\Delta\beta$, will determine the power transfer, which eventually leads to the optical modulation.

In this work, we deal with the semi-infinite coplanar strip (CS) electrode structure shown in Fig.7.1a. This electrode structure has been used for traveling-wave modulators/switches because of its low propagation losses, and easy launching of microwave signal from an external coaxial cable [19-22]. The electrode structure of Fig.7.1a can be modelled as a transmission line as illustrated in Fig.7.1b. When the electrodes have the same characteristic impedance as the source and termination, the modulation speed is limited only by the transit time difference between the optical and the modulating RF signals.

Calculations of the characteristic impedance for several different electrode structures with infinite thickness they electrodes have been

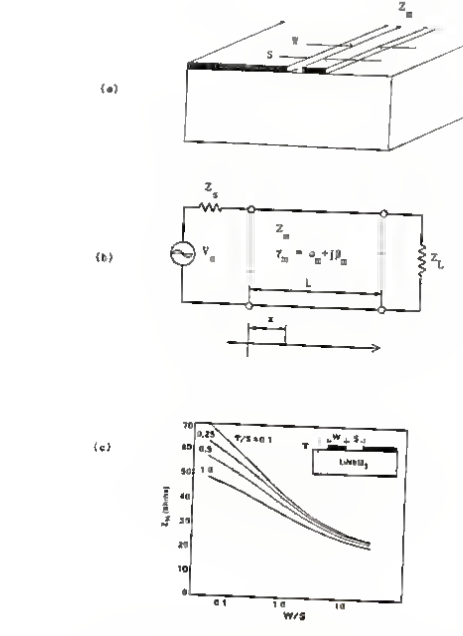

Fig.7.1 (a) Semi-infinite coplanar strip electrode configuration
(b) Equivalent transmission line
(c) Characteristic impedances vs. W/S

performed by the conformal mapping technique [56-59]. A quasi-static analysis through an integral equation [61] or the finite-difference method [17,48-50] were used to calculate the impedance of the semi-infinite CS electrode with finite thickness. The characteristic impedance Z_m is illustrated as a function of W/S with a parameter of electrode thickness in Fig.7.1e [61].

To be compatible with an external circuit, a characteristic impedance of 50 Ω is desirable. Because of the high index of $LiNbO_3$, the ratio of width to gap (W/S) needs to be around 0.2 to achieve 50 Ω when the electrode of typical thickness (T/S = 0.5) is used. From a practical point of view, it is hard to preserve the ratio of W/S all along the feeding, transmitting and terminating sections of the electrodes. In the feeding and terminating sections, it is easy to control the ratio of W/S arbitrarily. However, in the transmitting section, the electrodes gap needs to be about 3 μm to 7 μm. In order to meet the condition of W/S = 0.2 (50 Ω), one of the electrodes should be very narrow. This means that, if we fix W at 15 μm (which is the minimum width required to have no more than 1.5 $f^{1/2}$ dB/cm$(GHz)^{-1/2}$ of electrodes conducting loss), we need to have around 1 μm electrode width to maintain 50 Ω. This 1 μm is far narrower than 5 μm, a typical width of optical waveguides. Assuming W = 15 μm and S = 5 μm to achieve not only the proper overlap integral between optical and modulating microwave field but also an acceptable electrode conducting loss, the characteristic impedance of the asymmetric transmission line with T/S = 0.5 will be about 30 Ω.

Consider the transmission line of Fig 7.1b. The voltage distribution V(z) along the line is expressed as the sum of the forward and the backward traveling-waves.

$$V(z) = V_0 \frac{Z_{in}}{Z_{in}+Z_g} \left[\exp(-\gamma z) + \rho_L \exp(-\gamma L)\exp(\gamma(z-L)) \right]$$

$$= V_0 \frac{Z_{in}}{Z_{in}+Z_g} \left[\exp(-\gamma z) + \rho_L \exp(-2\gamma L)\exp(\gamma z) \right] \qquad (7.1)$$

where $\gamma_m = \alpha_m + j\beta_m$, $\rho_L = \frac{Z_L - Z_m}{Z_L + Z_m}$, $\beta_m = k_0 e_{eff}$, $Z_{in} = Z_m \frac{Z_L + Z_m \tanh(\gamma L)}{Z_m + Z_L \tanh(\gamma L)}$, α_m and β_m are the attenuation and the propagation constant of microwave. Z_g, Z_m, and Z_L are the microwave source impedance, the transmission section impedance and the terminating shunt load impedance, respectively. ρ_L is a reflection coefficient at $z = L$, $k_0 (= 2\pi f/c_0)$ is the wave number in the air, where c_0 is the light speed in vacuum, and V_0 is the open circuit driving voltage. The first term in the bracket of Eq. (7.1) is the forward traveling-wave while the second term is the backward traveling-wave.

The voltage V'(z) from the standpoint of the optical field propagating under the coplanar metal electrodes is given as

$$V'(z) = V(z)/\exp(-j\beta_{op}) = V_0 \frac{Z_{in}}{Z_{in}+Z_g} \left[\exp(pz) + \rho_L \exp(-2\gamma L)\exp(qz) \right] \qquad (7.2)$$

where $p = -\alpha_m + j(\beta_{op} - \beta_m)$ $\quad q = \alpha_m + j(\beta_{op} + \beta_m)$, $\quad \beta_{op} = k_0 n$.

We call ε_o and ε_{eff} the refractive index of an optical waveguide, and the effective dielectric constant in the microwave range. Note that $\varepsilon_o = 2.15$, $\varepsilon_{eff} = (1+\varepsilon_o \varepsilon_y)^{1/2} = 18.5$, where $\varepsilon_o = 43$ and $\varepsilon_y = 28$.

The overall refractive index change $\Delta n(f)$ induced by applied voltage is given by (20)

$$\Delta n(f) = \int_0^L V(z)dz = \frac{Z_{io}}{Z_{io}+Z_o}\left(\frac{\exp(\gamma L)-1}{\gamma} + \rho_L \exp(-2\gamma L)\frac{\exp(\gamma L)-1}{\gamma}\right) V_o \qquad (7.3)$$

The modulation depth $m(f)$ of the output intensity is expressed by

$$m(f) = \frac{\Delta n(f)}{\Delta n(0)} = \frac{Z_{io}}{Z_L}\frac{Z_L + Z_s}{Z_{io}+Z_o}\frac{1}{1+\rho_L}\left(\frac{\exp(\gamma L)-1}{\gamma L} + \rho_L \exp(-2\gamma L)\frac{\exp(\gamma L)-1}{\gamma L}\right] \qquad (7.4)$$

Equation (7.4) is the general expression for any type of traveling-wave electrode optical modulator regardless of the substrate material.

In the ideal case of $\alpha_m = 0$ and $Z_o = Z_m = Z_L$, Eq. (7.4) becomes

$$m(f) = \frac{\exp(\gamma L)-1}{\gamma L} = \exp(j\phi)\frac{\sin\phi}{\phi} \qquad \text{where} \quad \phi = \frac{\beta_{op} - \beta_m}{2} L \qquad (7.5)$$

In Fig.7.2a, with $\varepsilon_o = 2.15$ and $\varepsilon_{eff} = 18.5$ in $LiNbO_3$, the modulation depth $m(f)$ is plotted in Fig.7.2a as a function of frequency-length product for the ideal case of no loss ($\alpha_m = 0$) of Eq.(7.5). We note from the figure that $f_3 L = 6.5$ GHz-cm for 3 dB frequency-length product.

(a)

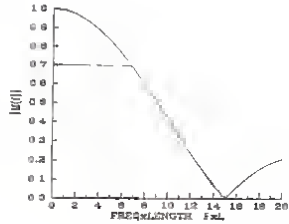

(b)

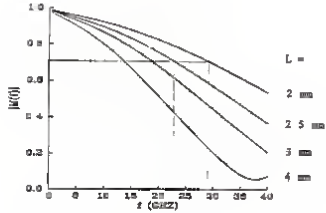

Fig.7.2 Modulation depth for (a) $\alpha_m = 0$, $Z_o = Z_m = Z_L$,
(b) $\alpha_m = 1.5$ dB/cm $GHz^{1/2}$ $Z_o = 50\ \Omega$, $Z_g = Z_L = 30\ \Omega$

The performance (especially the switching speed) of the traveling-wave optical switch is limited by several factors as we see in the Eq.(7.4). One is the impedance mismatch between Z_s, Z_m and Z_L, specially mismatch between Z_m and Z_L. The other factors are the velocity mismatch between the optical wave and modulating microwave $\beta_{op} - \beta_m$ and the microwave loss α_m along the electrodes. As a practical example, consider a semi-infinite CS electrode on $LiNbO_3$ with a 15 μm wide, 2.5 μm thick gold corrow electrode and a 5 μm gap, which is a typical example of a semi-infinite CS electrodes structure. The electrode conductor loss is such that $\alpha_m \sim 2.6\ f^{1/2}$ dB/cm(GHz)$^{-1/2}$ in the low-frequency range (less than 1 GHz), and $1.3\ f^{1/2}$ dB/cm(GHz)$^{-1/2}$ in the high-frequency range (above 4 GHz) [20,61]. In this simulation, we take $\alpha_m = 1.5$ dB/cm GHz$^{-1/2}$ in the high frequency range. The frequency response as a function of varying electrode lengths is drawn in Fig.7.2b based on Eq.(7.4). From the figure, we can see that the electrode length is one of the major factors that determine the performance of the optical modulators.

CHAPTER 5

DESIGN AND FABRICATION OF Y-BRANCH OPTICAL MODULATORS

Design of Y-branch Coupler and Electrodes

The optical modulator (Y-branch directional coupler and its corresponding electrodes) is drawn in Fig. 5.1 with all the details. The width of each of the optical waveguides is 5 μm and the directional coupler gap is 5 μm. Ti thickness prior to the diffusion is 700 A°. The diffusion is performed at 1025 $^{\circ}C$ for 6 hours. Based on the modeling results of the diffused index profile in Chapter 4, the calculation of coupling length of the device was done using a combination of the effective index method (EIM) and the finite difference method. In the calculation, the presence of the 1250 A° thick SiO_2 buffer layer was ignored and the values used were $\lambda = 1.3$ μm, and the $LiNbO_3$ refractive index $n_b = 2.15$. The calculation showed that the coupling length of the device was 2.17 mm.

The detailed procedure of calculating the Y-branch directional coupler's coupling length is as follows:

1. With a Ti diffusion condition of T = 1025 $^{\circ}C$, h = 6 hours, τ = 700 A° and a directional coupler's geometry of w = 5 μm and s = 5 μm, we obtain $d_x = d_y = 5.2$ μm, $\Delta n_c = 0.011$ from Eq. (4.14). We also obtain d = $w/d_x = 1.55$, e = $s/d_x = 1.55$, and $V_x = V_y = 3.40$ from Eqs. (5.14) to Eq. (5.23).

2. The above data are substituted into Eq. (5.24) and Eq. (5.25). The differential equation (5-24) is transformed to the integral form of

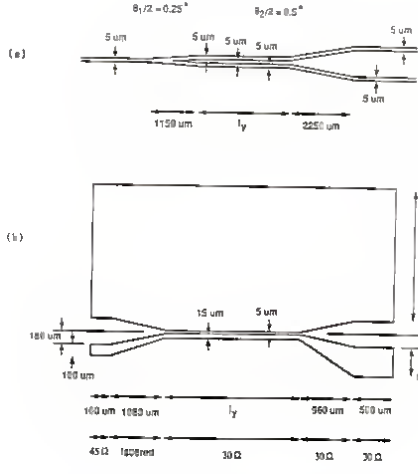

Fig. 1 (a) Detailed measure of the Y-branch directional coupler
(b) Detailed measure of the semi-infinite CS electrode

Eq.(3.26) by use of Eq.(3.9), the solution of Eq.(3.26) in Eq.(3.28). Substituting Eq.(3.28) back into Eq.(3.25) and solving Eq.(3.25) by use of 1-D FDM, we obtain even and odd fundamental modes' eigenvalues. Substituting the obtained eigenvalues into Eq.(3.30), we have the coupling length l_c = 3.07 cm.

3. The coupling length of the Y-branch coupler $l_y = l_c/\sqrt{2}$ = 2.17 cm is obtained from Eq.(3.22).

4. The overlap integral factor Γ_c = 0.515 is calculated from Eq.(3.2d) in case of the semi-infinite CS electrodes, where the modal widths of 1/e intensity are taken as $a_o = w_y \sim 2.5$ μm.

5. We finally obtain the switching voltage from Eq.(6.27) as

$$V_{sw} = 12.5 \text{ V} \quad \text{for} \quad l_y = 2.17 \text{ mm}.$$

We designed 1500 Å thick SiO_2 buffer layer on the substrate of optical waveguides to reduce the large optical loss due to the presence of the metal electrodes.

Travelling-wave electrode is employed to obtain high-speed modulation and large bandwidth. The semi-infinite coplanar strip (CS) electrode structure is chosen as a trade-off between impedance and resistance. Although the finite CS structure is feasible in adjusting the impedance between 30 Ω and 50 Ω, this structure tends to have high resistance due to its finite electrode width. By employing a semi-infinite CS structure, we lower the impedance slightly and reduce the resistance. The thickness of the Au electrodes is 2.5 μm. The source impedance of the microwave feeding coaxial

ochic ir 50 Ω. The impedance of the electrode input section is 45 Ω and is tapered to 30 Ω toward the main coupling section. The electrode gap is 5 μm and the width of the finite electrode is 15 μm. The impedance of the electrode main section is, therefore, 30 Ω from Fig 7 is used the feed impedance is also designed to be 30 Ω.

Fabrication of $LiNbO_3$ Optical Modulators

First, a cleaning procedure for Z-cut $LiNbO_3$ was performed using soap, Trichloroethane (TCE), Acetone, Methanol and DI water in sequence. Ti metal of 700 A^0 thickness was deposited on a z-cut $LiNbO_3$ substrate using the thermal evaporation deposition of Fig. 8.2. Standard photolithographic techniques were then used to form a photoresist pattern on the titanium film and a low-temperature wet-etching was used to remove the unwanted Ti metal from the surface. The photolithographic procedure is sketched in Fig 8.3. For diffusion, the temperature was ramped from room temperature to 1025 °C in a 4 hour period. The patterned Ti was in-diffused at 1025 °C for 6 hours. The furnace was allowed to cool passively to room temperature. To minimize the out-diffusion of Li and to ensure that the $LiNbO_3$ remains fully oxidized, wet O_2 was bubbled through deionized water at 70 °C and through the furnace tube at the rate of 2805 ml/min during the entire diffusion process. The diffusion process diagram is illustrated in Fig. 8.4.

To avoid the large optical loss that occurs when the quasi-TM mode optical field propagates under the metal electrodes, an intermediate dielectric buffer layer of SiO_2 is required between the optical waveguide

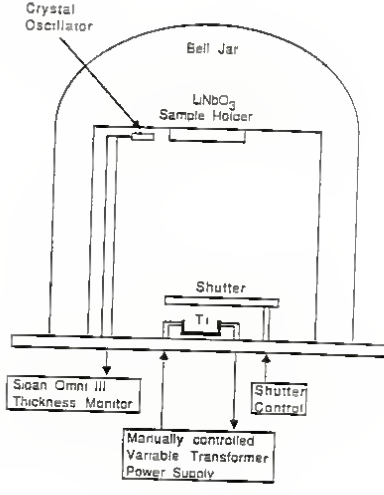

Fig.8.2 Thermal evaporation system for the deposition of thin film

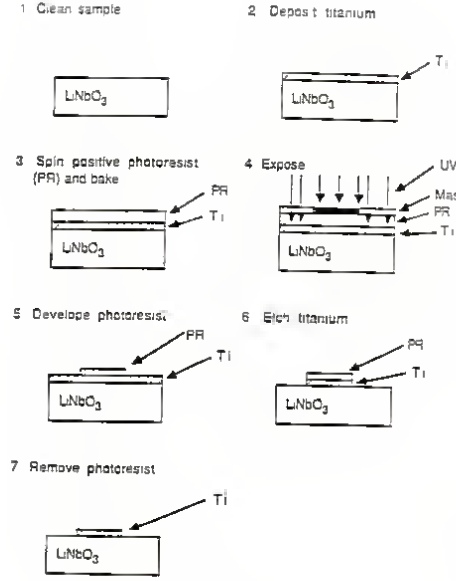

Fig 8.3 Photolithographic procedure

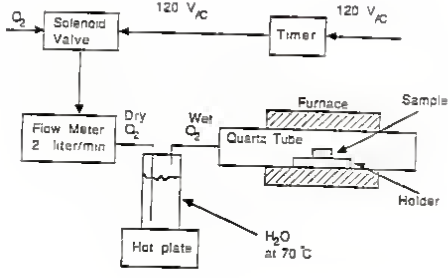

Fig.3.4 Diagram of diffusion process

and the metal electrode [5,62-64]. RF sputtering technique was used to deposit SiO_2 on the substrate. The RF incident power was 500 W and argon gas was flown at the rate of 20 cc/min. The pressure of the chamber due to the argon plasma was kept constant at 3 mmHg during the operation by controlling an orifice. The sputtering time was 35 min. and 1250 Å of SiO_2 film was deposited. However, the deposited SiO_2 film using RF sputtering has a potential problem of charge leakage through the dielectric buffer layer for low-frequency operation including dc operation [62]. Leakage current through this SiO_2 film originates from the incomplete oxidation of SiO_2. Such charge leakage can be eliminated by post-deposition annealing in an oxygen atmosphere [63] or by etching the buffer layer in the gap between the electrodes. Films of SiO_2 grown by chemical vapor deposition (CVD) eliminate such possibility of charge leakage thanks to the high quality of the SiO_2 film [5,24-64]. In our experiment, the device was annealed at 600 °C for 4 hours in an wet oxygen atmosphere to eliminate such leakage. We confirmed that there were no current leakages through the SiO_2 thin films for all devices.

Both ends of the device were polished to the order of 1/4 μm to enhance the coupling between the device and a fiber.

In order to pass the Al electrodes on the Y-branch directional coupler, the photoresist lift-off technique was used at first. In this technique, the cleaning procedure and the procedure for removing moisture are very important. The processing data in the lift-off technique such as pre- and post-baking time, UV exposure intensity, exposure time, and developing time were not consistent in achieving a clean metal pattern. The procedure was

not reproducible as mentioned in Elliott [65]. The etching technique was then used to fabricate the electrodes after thin film of Al was deposited on the SiO_2 film.

CHAPTER 9

MEASUREMENT AND RESULTS

The final devices for the test are illustrated in Fig.9.1. Figure 9.1a is for the dc test and Fig.9.1b is for the microwave test. The modulator was evaluated at 1.3 μm wavelength for quasi-TM mode. The light was coupled into a polished waveguide input end, then, coupled out of the other waveguide ends to the detector by use of a focusing lens. The dc switching test for the device was carried out.

The block diagram for the optical measurement is sketched in Fig.9.2. Using this test set-up, we first measured the optical mode profiles, which are plotted in Fig.9.3. The quasi-TM mode of each waveguide showed, in 1/e intensity, a modal depth of 3.48 μm and a modal width of 4.95 μm. The calculation by the 2-D FDM showed that the modal depth was 3.20 μm and modal width was 4.66 μm. Field profiles from both waveguides output were confirmed to be symmetric.

Two samples were tested for dc switching operation. In Fig.9.4, the simulated power output $\int(x)R^{*}(x)$ of Eq.(6.25) is drawn with a parameter of the interaction length L, which is based on Eq.(6.8). The measured data for the two samples are also illustrated in Fig.9.4. From the figure, we can estimate the extinction ratio. On the other hand, from Fig.7.2b in Chapter 7, we see the frequency response of the modulation depth with a parameter of the interaction length, which is calculated from Eq.(7.4). Using this

(a)

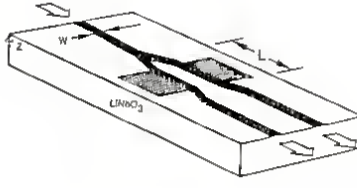

(b)

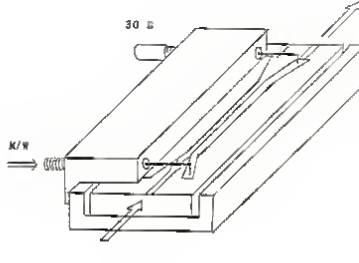

Fig. 1 $LiNbO_3$ optical modulators for (a) dc test, (b) RF test

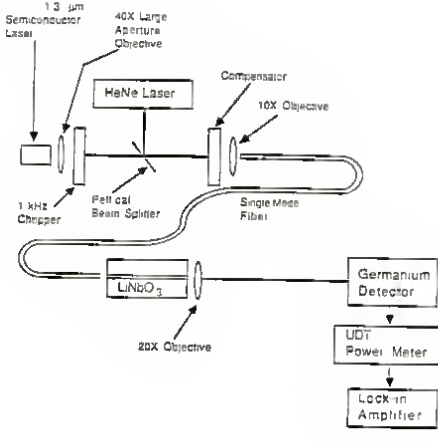

Fig-9 2 Block diagram for the dc test and the near-field measurement

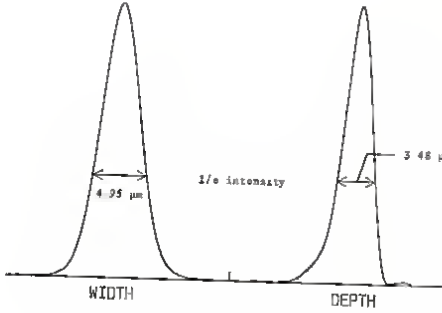

Fig 9 3 Measured field profiles (a) Horizontal, (b) Vertical

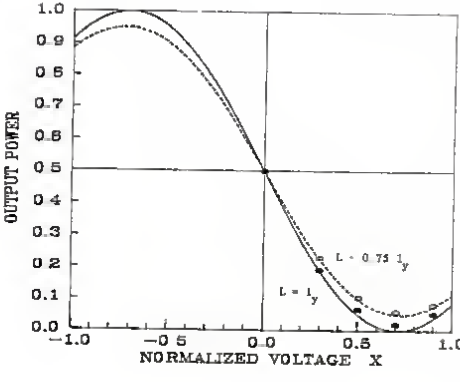

Fig 9.4 Calculated (lines) and measured (dots) power output RR* solid (for L = l_y), dashed (for L = 0.75 l_y)

equation, we can estimate the expected bandwidth of the device. We summarize the above results as follows:

Device length	$L = l_y$	$L = 0.75\ l_y$
Switching voltage	12.5 V	20 V
Extinction ratio	17 dB	13 dB
Expected bandwidth	17 GHz	23 GHz

The dc test showed that the actual Y-branch device's coupling length l_y was around 3.25 mm, while the calculated coupling length was 2.17 mm. The source of the error can be interpreted from both theoretical and experimental points of view. Theoretically, the deviation could have been caused from the error in calculating the coupling length by the effective index method, and from the error caused by ignoring the presence of the SiO_2 buffer layer. Experimentally, there are several potential points where errors may occur: over- or under-developing of the photoresist, and over- or under-etching of the Ti patterns. Even with a perfect design of a device's interaction length, there should be minor coupling at the gradually branching-out section of the coupler's output.

For the RF test, we chose $L = 0.75\ l_y$. This selection gives the good compromise between the large bandwidth (high-speed), the high extinction ratio, and the high switching voltage. Since we emphasized the large bandwidth, the device of $0.75\ l_y$ was chosen at the cost of having the high switching voltage and the low extinction ratio. The microwave test will be conducted in the near future.

CHAPTER 10

SUMMARY AND DISCUSSION

In designing optical modulators and switches, there are three factors that determine the ultimate performance of the Ti-indiffused $LiNbO_3$ modulators: bandwidth (high speed), switching voltage and extinction ratio. It is, however, difficult to design a practical device with good overall performance in all of the three parameters. For example, the bandwidth can be improved at the expense of switching voltage by shortening the coupling length of the device. Shortening the coupling section is achieved by reducing the electrode gap which in turn degrades the extinction ratio. Therefore, there needs to be trade-off to produce a device with superior performance in some particular aspects.

Several types of optical modulators including the cut-off, the uniform directional coupler (DC), Mach-Zehnder interferometer, the alternating $\Delta\beta$ DC, the cross coupler and the Y-branch DC were presented and discussed. The Y-branch directional coupler, among them, was the most promising not only because the device's coupling length is about 70% of that of the uniform DC, but also because it is easy to employ the travelling-wave electrodes. Reduction of the coupling length is very advantageous in achieving high-speed operation. This is the main reason why we selected this type of modulator to obtain a large bandwidth.

In this work we have developed several analytical and numerical methods: i) general WKB theory for the analysis of arbitrarily graded-index

waveguides including directional couplers 2) 2-D finite difference method (2-D FDM) for both analysis and modelling of waveguides 3) conformal mapping technique to solve several kinds of electrode structures 4) traveling-wave analysis to calculate the modulation depth.

Based on the developed theories and numerical techniques above, Y-branch directional coupler optical modulators using traveling-wave electrodes were designed, fabricated and tested.

In Chapter 2, the material properties of $LiNbO_3$ and GaAs were compared from the viewpoint of high-speed optical modulation. Several factors including the loss, the electro-optic effect, and the velocity mismatch between the RF field and the optical field were discussed to evaluate the general performance of the optical modulator. The results indicated that $LiNbO_3$ is more suitable for high-speed modulators using traveling-wave electrodes. It is, however, hard to consider which material is superior since GaAs appears to be a better position from the viewpoint of optical circuit integration.

In Chapter 2, we have discussed the effective index method (EIM) and evaluated its particular error, especially near the cut-off region. The results of EIM were compared with those of 2-D FDM. The results indicate that EIM shows a large error around the fundamental mode cut-off region. However, EIM results for the well-guided fundamental mode, i.e., near the second mode cut-off region, are quite accurate. This fact is very important from a practical point of view.

In Chapter 3, the general eigenvalue equations of WKB theory were derived to solve the wave equation for arbitrarily graded-index directional couplers.

The theory is utilized for the coupling length calculations of directional couplers with aid of the EIM.

In Chapter 4, nonuniformly discretized 2-D FDM was developed to model a diffusion profile of a channel waveguide. The method took into account boundary conditions either for quasi-TM mode or for quasi-TE mode. The flexible discretization enabled us to put a metal box far away from the guiding region with a limited number of grid lines. The guiding region was sliced minutely, while the region outside was sliced more sparsely. Matrix size and corresponding computing time were reduced considerably. In the modeling, diffusion lengths in lateral and depth directions were also extracted to fit experimental results of mode profiles.

In Chapter 5, the conformal mapping technique was developed to find the static electric field distribution generated by the applied voltage on the electrodes. The method was powerful in that the field analysis is applicable even to the general cases of anisotropic materials. The analytical procedures were applied to find an optimal overlap integral between the modulating RF electric field and the propagating optical field. For the CS electrode, the maximum overlap integral occurred when the inner edge of the electrode was positioned in alignment with the inner edge of the Ti strip prior to the diffusion.

In Chapter 6, the coupled mode theory was utilized to explain the coupling phenomena in various coupled structures. The transfer matrix was derived in the normalized form relating both input port and output port of the device. The coupling length of the Y-branch directional coupler was compared with that of the uniform DC in case for the same channel width and

gap. The fact that the coupling length of the Y-branch directional coupler is about 70% of that of the uniform case is very important for high-speed operation.

In Chapter 7, wave behavior in a travelling-wave electrode was analyzed to calculate the modulation depth using a transmission line theory. The modulation depth is a function of source impedance, line impedance of a coupling section, load impedance, optical and microwave index of $LiNbO_3$, coupling length and microwave frequency. The band-width of an optical modulator could be predicted through the analysis.

In Chapter 8, based on the above discussion and theoretical analyses obtained, we designed a Y-branch directional coupler $LiNbO_3$ optical modulator with a travelling-wave electrode. We employed the travelling-wave electrode of a semi-infinite coplanar strip (CS) in order to achieve high-speed switching operation. The fabrication procedure for the designed optical modulators are described in detail.

In Chapter 9, the measurement and the results were presented. Using the optical measurement set-up of Fig. 9.2, dc switching operation was tested. The optical field intensities of each channel waveguide were first measured. The Y-branch directional coupler is basically a 1x2 half biased switch. Without any applied voltage, the output field profiles of the two arms of the Y-branch directional coupler need to be symmetric. This symmetry and the switching operation were successfully confirmed.

There were many obstacles in performing the several steps of fabrication. We have experienced two especially troublesome steps; depositing the SiO_2 buffer layer using E-beam technique, and making the Al electrode pattern

oolop the lift-off technique. Three ways of depositing SiO_2 were available liquid phase chemical vapor deposition (LPCVD), electron beam (E-beam) deposition and RF sputtering. We first tried E-beam deposition for depositing a thin SiO_2 layer. Even if we tried to bombard the SiO_2 source at the lowest speed (1-4 A°/sec) by a high energy electron beam, the deposited thin film appeared to be coarse. When the samples were soaked in acetone for the next step, the thin film immediately showed cracks. As this phenomenon happened repetitively, we gave up trying this technique and changed to the RF sputtering technique. The deposition rate depended on Argon flow rate, chamber pressure of Argon plasma, and incident microwave power. The deposition rate was kept at around 35 A°/min. by controlling a chamber orifice. The deposited SiO_2 were very stable and the samples were annealed at 600 C° for 4 hours to remove the possibility of a charge leakage.

In putting the semi-infinite CS electrodes on the Y-branch directional coupler, the lift-off technique was used first. In this technique, a cleaning procedure and a step to remove moisture were extremely important. Even with small amount of moisture, some part of Al patterns turned out to be lifted. The processing parameter in the lift-off technique such as pre- and post-baking time, UV exposure intensity, exposure time, and developing time were not consistent in achieving a clean Al pattern. The etching technique was then used to obtain the nine electrode patterns. The clean Al patterns could be obtained with an yield of almost 100%.

From the dc test, the actual coupling length l_y was proved to be around 3.25 mm rather than a theoretically estimated value of 2.17 mm. The

discrepancy between the calculated coupling length and the fabricated device can be attributed to both theoretical and experimental reasons. In theoretical calculation, the deviation might be caused from the error in calculating the coupling length by the effective index method and from the error caused by ignoring the presence of the SiO_2 buffer layer. However, the dominant causes of the deviation might result from the fabrication procedure in experiment. The potential causes in experiment are over- or under-developing of the photoresist and over- or under-etching of the Ti pattern. These kinds of errors change the channel width and channel gap at the same time, which effect a strong influence on the actual coupling length. Even with a perfect design of a device's interaction length, some power transfer still occurs in the gradually tapered section of the coupler's output.

In testing the dc switching operation, applied voltage on the electrodes were varied from 0 V to 50 V. Two devices were tested in the dc switching i_y and 0.75 i_y. The experiment showed that, for the interaction length of i_y, the switching voltage was 12.5 V, and the extinction ratio was 17 dB. For the device of 0.75 i_y, the switching voltage and the extinction ratio were 20 V and 13 dB, respectively.

For the microwave test, the device of 0.75 i_y was chosen. The selection was made at the cost of increasing the switching voltage and lowering the extinction ratio since we emphasized the high-speed modulation. The estimated bandwidth of the device of 0.75 i_y is 23 GHz, while that of the device of i_y is 17 GHz. The microwave test will be conducted in the near future.

APPENDIX A

CONFORMAL MAPPING FUNCTIONS

From Eq. (5.3) and Eq(5.7),

$$\frac{dw}{dz} = \frac{[(a-c)(b-d)]^{1/2}}{(z-a)^{1/2}(z-b)^{1/2}(z-c)^{1/2}(z-d)^{1/2}} \tag{A.1a}$$

$$a_0 = j2K(k') = jK'(k) \tag{A.1b}$$

$$c_0 = 2K(k) \tag{A.1c}$$

where

$$k = \left[\frac{(b-c)(a-d)}{(a-c)(b-d)}\right]^{1/2}, \quad k' = [1 - k^2]^{1/2}$$

Symmetric CS or CCS Electrodes ($a + d = 0$, $b + c = 0$)

Inserting the conditions, $a + d = 0$ and $b + c = 0$ into Eqs.(A.1)

$$\frac{dw}{dz} = \frac{(a+b)}{(z^2-a^2)^{1/2}(z^2-b^2)^{1/2}} \tag{A.2a}$$

$$a_0 = jK(k) \tag{A.2b}$$

$$c_0 = 2K(k') = 2K'(k) \tag{A.2c}$$

where $k = (a - b)/(a + b)$

or, $k = W/(W + S)$ in the symmetric CS

$= S/(W + S)$ in the symmetric CCS

W is the electrode width and S is the gap between the electrodes. We can verify that Eqs.(A 2) can be rewritten into equivalent forms by use of the elliptic function identity

$$w = \int_b^a \frac{(a + b)}{(a^2-z^2)^{1/2}(z^2-b^2)^{1/2}}\,dz = \int_1^{a/b} \frac{dt}{(1-t^2)^{1/2}(1-k^2t^2)^{1/2}} \qquad \text{(A 3a)}$$

$$\theta_0 = jK(k') = jK(k) \qquad \text{(A.3b)}$$

$$s_0 = 2K(k) \qquad \text{(A 3c)}$$

where $k = b/a$ and $z = sn(w,k)$ sine amplitude function

or, $k = S/(2W + S)$ in the symmetric CS,

$= W/(2S + W)$ in the symmetric CCS,

Semi-Infinite Electrodes ($d = -\infty$, $c = 0$)

Dividing both numerator and denominator of Eq.(A-1a) by $(-d)^{1/2}$ and setting $d = -\infty$ and $c = 0$, we have

$$w = \int_b^{\infty} \frac{z^{1/2}}{(z-a)^{1/2}(z-b)^{1/2}\,z^{1/2}}\,dz = \int_1^{(z/b)^{1/2}} \frac{dt}{(1-t^2)^{1/2}(1-k^2t^2)^{1/2}} \qquad (A.4a)$$

$$w_0 = jK(k') = jK'(b) \qquad (A.4b)$$

$$w_0 = 2K(k) \qquad (A.4c)$$

where $b = (b/a)^{1/2}$ and $x = b\,sn^2(\frac{w}{2}, k)$

Two-Infinite Electrodes ($a + d = 0$, $b + c = 0$, $a = \infty$)

This case is a special one for the symmetric CS finite electrodes. Dividing the numerator and denominator of Eq (A.2a) by a, and setting $a = \infty$, we obtain

$$w = \int_b^{x} \frac{1}{(x^2-b^2)^{1/2}}\,dx = \cosh^{-1}\left(\frac{x}{b}\right) \qquad (A.5a)$$

From Eq.(A.2b) and Eq.(A.2c), and taking $a = \infty$

$$w_0 = jK(1) = j\infty \qquad (A.5b)$$

$$w_0 = 2K(0) = \pi \qquad (A.5c)$$

APPENDIX B

PERTURBATION THEORY

A formalism of directional coupling between two adjacent waveguides can be developed from the Maxwell's wave equation of the form

$$\nabla^2 E(x,t) = \mu \frac{\partial^2}{\partial t^2} (\varepsilon(x) E(x,t)) = \mu \frac{\partial^2}{\partial t^2} [\varepsilon_0 E(x,t) + P(x,t)] \tag{B.1}$$

and
$$P(x,t) = P_0(x,t) + \Delta P_0(x,t) \tag{B.2a}$$

$$P_0(x,t) = (\varepsilon(x) - \varepsilon_0) E(x,t) \tag{B.2b}$$

$$\Delta P_0(x,t) = \Delta\varepsilon(x) E(x,t) = \Delta n^2(x) \varepsilon_0 E(x,t) \tag{B.2c}$$

where $P_0(x,t)$ and $P(x,t)$ are the unperturbed and the perturbed polarizations, respectively, in the guided structure. A transverse modal field $E(x,t)$ is one of these components in the rectangular coordinate and $P(x,t)$ is the component in the same polarization. Substituting Eqs.(B.2) into Eq (B.1), we obtain

$$\nabla^2 E(x,t) - \mu\varepsilon(x) \frac{\partial^2}{\partial t^2} E(x,t) = \mu \frac{\partial^2}{\partial t^2} [\Delta P(x,t)] \tag{B.3}$$

Under the assumption that there is no variation of index in y-direction ($d/dy = 0$), we can expand the total field in the perturbed waveguide as a superposition of confined modes,

$$E(x,t) = \sum_m C_m(z)\, E_m(x) e^{j(\omega t - \beta_m z)} \qquad (B.4)$$

where $E_m(x)$ satisfies

$$\left(\frac{\partial^2}{\partial x^2} - \beta_m^2\right) E_m(x) + \omega^2 \mu\varepsilon(x) E_m(x) = 0 \qquad (B.5)$$

Substitution of Eq. (B.4) in Eq. (B.3) leads to

$$e^{-j\omega t} \sum_m C_m(z)\left[\left(\frac{\partial^2}{\partial t^2} - \beta_m^2\right) E_m(x) + \omega^2 \mu\varepsilon(x) E_m(x)\right] e^{-j\beta_m z} + \left[-j2\beta_m \frac{d}{dz} C_m(z) + \frac{d^2}{dz^2} C_m(z)\right] E_m(x) e^{-j\beta_m z} = \mu \frac{\partial^2}{\partial t^2}[\Delta P(x,t)] \qquad (B.6)$$

Note that the sum of the first three terms in Eq. (B.6) is zero in view of Eq. (B.5). If we assume slowly varying inhomogeneity, i.e., $\lambda \left|\partial A^2/\partial x^2\right| \ll \partial A/\partial z$, Eq. (B.6) reduces to the approximate form

$$-\sum_m j2\beta_m \frac{d}{dz} C_m(z) E_m(x) e^{j(\omega t - \beta_m z)} = \mu \frac{\partial^2}{\partial t^2}[\Delta P(x,t)] \qquad (B.7)$$

We take the product of Eq. (B.7) with $E_n(x)$. Then,

$$-\sum_m j2\beta_m \frac{d}{dz} C_m(z) E_m(x) E_n(x) e^{j(\omega t - \beta_m z)} = \mu \frac{\partial^2}{\partial t^2}[\Delta P(x,t) E_n(x)] \qquad (B.8)$$

With the orthogonality condition [40] of

$$\frac{1}{2}\int_{-\infty}^{\infty} E_m(x)E_n(x)dx = \frac{\beta}{2\omega\mu}\int_{-\infty}^{\infty} E_m(x)E_c(x)dx = \delta_{mn} \qquad (B.9)$$

where δ_{mn} is Kronecker delta, so integrate Eq. (B.9) from $-\infty$ to ∞. Thus,

$$\frac{d}{dz}C_n(z)e^{j(\omega t-\beta_n z)} - \frac{d}{dz}C_{-n}(z)e^{j(\omega t+\beta_n z)} = \frac{j}{4\omega}\frac{\partial^2}{\partial t^2}\int_{-\infty}^{\infty} \Delta P(x,t)E_n(x)dx \qquad (B.10)$$

Here we deal with the case of forward co-directional interaction only. Thus, Eq. (B.10) becomes

$$\frac{d}{dz}C_n(z)e^{j(\omega t-\beta_n z)} = \frac{j}{4\omega}\frac{\partial^2}{\partial t^2}\int_{-\infty}^{\infty} \Delta P(x,t)E_n(x)dx \qquad (B.11)$$

Consider the case of two planar waveguides illustrated in Fig. B.1. The refractive index distribution for each waveguide in the absence of the coupling is given by $n_1(x)$ and $n_2(x)$. The corresponding fields are denoted by E1(x) and E2(x). In most cases, the perturbation is small and the overall field in the guiding structure can be represented by the combined fields, E1(x), and E2(x), the local normal modes of the two isolated guides.

$$E(z) = A(z)E1(x)e^{j(\omega t-\beta_1 z)} + B(z)E2(x)e^{j(\omega t-\beta_2 z)} \qquad (B.12)$$

where β_1 and β_2 are the propagation constants of each waveguide. The perturbation polarization responsible for the coupling is calculated by substituting Eq. (B.12) into Eq. (B.2c). The result is

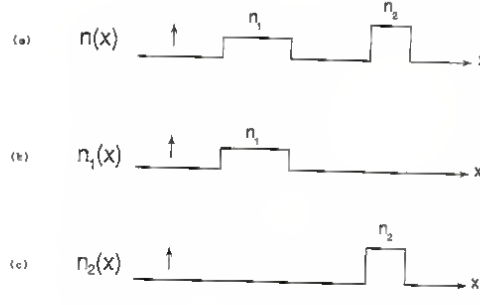

Fig.B.1 Refractive index profiles (a) Directional coupler n(x)
(b) (c) Isolated waveguides $n_1(x)$ and $n_2(x)$

$$\Delta P_e = e^{j\omega t} e_x [A(z)E1(x)(n^2(x)-n_1^2(x))e^{-j\beta_1 x} + B(e)E2(x)(n^2(e)-n_2^2(e))e^{-j\beta_2 z}] \tag{B.13}$$

By replacing $E_x(x)$ of Eq (B.11) with E1(x) and E2(e), respectively, Eq. (B.11) reduces to two separate equations:

$$\frac{\partial}{\partial e}A(e)e^{j(\omega t-\beta_1 x)} = \frac{j}{4\omega}\frac{\partial^2}{\partial t^2}\int_{-\infty}^{\infty}\Delta P(x,t)E1(e)dx \tag{B.14a}$$

$$\frac{d}{dx}B(x)e^{j(\omega t-\beta_2 e)} = \frac{j}{4\omega}\frac{\partial^2}{\partial t^2}\int_{-\infty}^{\infty}\Delta P(x,t)E2(e)dx \tag{B.14b}$$

Note that the complex amplitude A(z) and B(e) replace $C_n(z)$ of Eq. (B.11) in formulating Eqs.(B.14). Substitution of Eq. (B.13) into Eqs.(B.14) leads to

$$\frac{\partial}{\partial e}A(z) = -jk_{12}B(z)e^{j(\beta_1-\beta_2)e} - jM_1A(z) \tag{B.15a}$$

$$\frac{d}{de}B(e) = -jk_{21}A(z)e^{j(\beta_2-\beta_1)z} - jM_2A(z) \tag{B.15b}$$

where

$$k_{12} = \frac{\omega\varepsilon_0}{4}\frac{\partial^2}{\partial t^2}\int_{-\infty}^{\infty}(n^2(x)-n_2^2(x))E1(x)E2(x)dx \tag{B.16a}$$

$$k_{21} = \frac{\omega\varepsilon_0}{4}\frac{\partial^2}{\partial t^2}\int_{-\infty}^{\infty}(n^2(x)-n_1^2(x))E2(e)E2(e)de \tag{B.16b}$$

$$M_1 = \frac{\omega\varepsilon_0}{4}\frac{\partial^2}{\partial t^2}\int_{-\infty}^{\infty}[\varepsilon^2(x)-\varepsilon_1^2(x)][E1(x)]^2dx \qquad (B.16c)$$

$$M_2 = \frac{\omega\varepsilon_0}{4}\frac{\partial^2}{\partial t^2}\int_{-\infty}^{\infty}[\varepsilon^2(x)-\varepsilon_2^2(x)][E2(x)]^2dx \qquad (B.16d)$$

Since we deal with the weak coupling, M_1 and M_2 are almost negligible. Ignoring M_1 and M_2, we finally have

$$\frac{d}{dx}A(x) = -jk_{12}B(x)e^{-j\Delta\beta x} \qquad (B.17a)$$

$$\frac{d}{dx}B(x) = -jk_{21}A(x)e^{j\Delta\beta x} \qquad (B.17b)$$

where $\Delta\beta = \beta_2 - \beta_1$.

REFERENCES

1. I.P. Kaminow and R.V. Ramaswamy, 'Lithium niobate ridge waveguide modulator,' Appl. Phys. Lett., Vol.24, No.12, p.622, 15 June 1974

2. R.V. Ramaswamy, M.R. Davino and R.B. Stanley, 'Balanced bridge modulator switch using Ti-diffused $LiNbO_3$ strip waveguides,' Appl. Phys. Lett., Vol.32, No.10, p.644, 15 may 1978

3. E. Auracher and H. Keil, 'Design considerations and performance of Mach-Zehnder waveguide modulator', Revue Electron., Vol.4, p.129, 1980

4. D.W. Dolfi, 'Traveling-wave 1.3 μm interferometer modulator with high bandwidth, low driver power, and low loss,' Appl. Optics, Vol.25, No.15 p.2479, 1 August 1986

5. Y. Gourhia, M. Papuchon, E.M. Werner and C. Meroswalle, 'Intrinsically resonant traveling-wave Y-fed directional couplers at high frequency,' Appl. Phys. Lett., Vol.53, No.20, p.1964, 14 November 1988

6. J.C. Campbell, F.A. Blum, D.W. Shaw and K.L. Lawley, 'GaAs electrooptic directional coupler switch,' Appl. Phys. Lett., Vol.27, No.4, p.202-1975

7. F.J. Leonberger, J.P. Donnelly and C.O. Bozler, '$GaAs$ $P^{+}n^{-}n^{+}$ directional coupler switch,' Appl. Phys. Lett., Vol.29, No.10, p.652, 1976

8. N. Kamegachi, 'GaAs rib-waveguide directional coupler switch with Schottky barrier,' Electron. Lett., Vol.14, No.13, p.387, 22 June 1978

9. J.P. Donnelly, N.L. Demao, G.A. Ferrante and K.B. Nichols, 'A high frequency GaAs optical guided-wave electrooptic interferometric modulator,' IEEE J. Quantum Electron., Vol. QE-21, No.1, p.18, January 1985

10. S.K. Wang, 'High-speed III-V electrooptic waveguide modulators at 1.3 μm' IEEE J. Lightwave Technol., Vol LT-4, No.6, p.758, June 1986

11. R. Inoue, K. Kimura, K. Ishida, T. Asai and H. Matsumura, 'Low-loss GaAs optical waveguides,' IEEE J. Lightwave Technol., Vol LT-3, No.3, p.1270, 1985

12. P. Suchosky and R.V. Ramaswamy, 'Minimum mode-size, low-loss Ti:$LiNbO_3$ channel waveguides for efficient modulator operation at 1.3 μm,' IEEE J. Quantum Electron., Vol QE-23, No.10, p.1673, October 1987

13. W.K. Burns, P.H. Klein and E.J. West, 'Ti diffusion in Ti:$LiNbO_3$ planar and channel optical waveguides,' J Appl. Phys., Vol.50, No.10, p 6175, October 1979

14. M. Minakata, S. Saito and S. Miyaruma 'Two dimensional distribution of refractive index changes in Ti-diffused $LiNbO_3$ strip waveguides,' J. Appl. Phys., Vol.50 No.5, p.3063, May 1979

15. H. Fukuma and J. Noda,'Optical properties of Ti-diffused $LiNbO_3$ strip waveguides and their couplings-to-a-fiber characteristics', Appl. Opt., Vol.19, No.4, p.591, 15 February 1980

16. J. Čtyroký, M. Hofman J. Janta and J. Schrofel,'3-D Analysis of $LiNbO_3$ Ti channel waveguides and directional couplers,' IEEE J. Quantum Electron., Vol QE-20, No.4, p.400, April 1984

17. C.M. Kim and K.V. Ramaswamy,'Modeling of Graded-Index channel waveguide using a non-uniform finite-difference method,' IEEE J. Lightwave Technol., Vol.LT-7, No.10, October 1989

18. S. Steffen, A. Meyer and E. Voges,'Direct measurement of refractive index profiles of Ti:$LiNbO_3$ planar and strip waveguides by reflectivity profiling,' IGWO Conference, Vol.4, p.121, February 1989

19. S.K. Korotky, G. Eisenstein, R.S. Tucker, J.J. Veselka and G. Raybon,' Optical intensity modulation to 40 GHz using a waveguide electro-optic switch,' Appl. Phys. Lett., Vol.50, No.23, p 1631, 8 June 1987

20. K. Kubota, J. Noda and O. Mikami,'Traveling-wave optical modulator using a directional coupler $LiNbO_3$ waveguide,' IEEE J. Quantum Electron., Vol QE-16, No.7, p.754, July 1980

21. R.C. Alferness, C.H. Joyner, L.L. Buhl and S.K. Korotky,'High-speed traveling-wave directional coupler switch/modulator for $\lambda = 1.32$ μm' IEEE J. Quantum Electron., Vol QE-19, No.9, p.1339, September 1983

22. H. Nagu, M. Izutsu and T. Sueta,' $LiNbO_3$ traveling-wave light modulator/switch with an etched groove,' IEEE J. Quantum Electron., Vol.QE-22, No.6, p.932, June 1986

23. A. Meyer and W. Sohler,'High-speed cutoff modulator using a Ti-diffused $LiNbO_3$ channel waveguide,' Appl. Phys Lett., Vol.35 No.8, p.256, 1 August 1979

24. R.V. Schmidt and K. Kogelnik, 'Electro-optically switched coupler with stepped $\Delta\beta$ reversal using Ti-diffused $LiNbO_3$ waveguides,' Appl. Phys Lett., Vol.28, No.9, p 503, 1 May 1976

25. H. Kogelnik and R.V. Schmidt,'Switched directional couplers with alternating Δβ,' IEEE J. Quantum Electron., Vol.QE-12, No.7, p.396, July 1976

26. A. Neyer,'Electro-optic x-switch using single mode Ti:$LiNbO_3$ channel waveguides,' Electron. Lett., Vol.19, No.14, p.553, 1983

27. K. Goel, E. Wooten and W.S.C. Chang,'Design considerations for low switching voltage crossing channel switch,' IEEE J. Lightwave Technol., Vol.LT-6, No.6, p.881, June 1988

28. S. Thaniyavarn,'Modified 1x2 directional coupler waveguide modulator,' Electron. Lett., Vol.22, No.18, p.941, 28 August 1986

29. S. Thaniyavarn,'Modulation Allgrome of coupled-waveguide interferometers and directional couplers,' SPIE Vol.835, Integrated Optical Circuit Eng. V, p.197, 1987

30. R.M. Bowerton, C.E. Palmer and W.K. Burns,'Characterization of a self biased linear 1x2 directional coupler,' SPIE Vol.835, Integrated Optical Circuit Eng. V, p.126, 1987

31. E.A.J. Marcatili,'Dielectric rectangular waveguide and directional coupler for integrated optics,' Bell syst. Tech. J., Vol.48, p.2071, September 1969

32. J.E. Goell,'A circular-harmonic computer analysis of rectangular dielectric waveguides,' Bell syst. Tech. J., Vol.48, p.2133, September 1969

33. R.M. Knox and P.P. Toulios,'Integrated circuit for the millimeter through optical range,' Proceedings of MRI Symposium on Submillimeter Waves, p.497, J. Fox,Ed. Brooklyn: Polytechnic Press, 1970

34. K.V. Ramaswamy,'Strip-loaded film waveguide,' Bell Syst. Tech. J., Vol.53, No.4, p.697, April 1974

35. G.B. Hocker and W.K. Burns,'Mode dispersion in diffused channel waveguides by the effective index method,' Appl. Optics, Vol.16, No.1, p.113, January 1977

36. C.H. Kim and K.V. Ramaswamy,'WKB Analysis of Asymmetric Directional Couplers and Its Application to Optical Switches,' IEEE J. Lightwave of Technol., Vol.LT-6, No.6, p.1139, June 1988

37. A. Hamer, B.F. Clark and B. Culshaw, Explanation of errors inherent in the effective index method for analyzing rectangular-core waveguides,' Optics Lett., Vol.13, No.12, p.1122, December 1988

38. C B. Kim, S G Jang and C M Lee 'Analysis of dielectric rectangular waveguide by the modified effective index method' Electron. Lett. Vol.22, No 6, p 296, Mar. 1986

39. S E, Miller,'Integrated optics: An introduction,' Bell Syst.Tech.J., Vol 48, p.2071, 1969

40. A Yariv.'Coupled mode theory for guided wave optics,' IEEE J Quantum Electron , Vol QE-9, No.9, p.919, September 1973

41 E Marom, O.O. Ramer and S. Ruschin,'Relation between normal-mode and coupled-mode analyses of parallel waveguides,' IEEE J. Quantum Electron., Vol.QE-20, No.12. p.1311, December 1984

42 L Tsang and S.L. Chuang, 'Improved coupled mode theory for reciprocal semistropic waveguides,' IEEE J, Lightwave Technol , Vol.LT-6, No.2. p.304, February 1988

43. K.Thyagarajan, A.Kumar and I C, Goyal,'Exact analysis of the evanescent coupling between two indiffused optical waveguides,' Applied Optics, Vol 20, No 10, p.1821, May 1981

44. J.L Powell and B. Crossmann, Quantum Mechanics, Reading, MA: Addison Wesley, 1961

45. M. Abramowitz and I.A Stegun, Handbook of Mathematical Function. New York: Dover Publications Inc., 1970

46. M.J. Adams, An introduction to Optical Waveguides, New York Wiley Interscience, 1988

47. H.A. Haus, W, Huang, N.M. Whitaker,'Optical Waveguide Dispersion Characteristics from the Scholer Wave Equation,' IEEE J. Lightwave Technol., Vol LT-5, No.12, p.1748, December 1987

48. E, Schaelg, W B, Bridges,'Computer Analysis of Dielectric Waveguides: A Finite-Difference Method,' IEEE Trans. Microwave Theory Tech., Vol.MTT-32, No.5, p.531, May 1984

49. K. Bierwirth, N Schulz and F. Arndt 'Finite-Difference Analysis of Rectangular Dielectric Waveguide Structures,' IEEE Trans Microwave Theory Tech , Vol.MTT-34, No.11, p.1104, November 1986

50. M S, Stern,'Semivectorial polarized finite difference method for optical waveguides with arbitrary index profile,' IEE Proceedings, Vol 135, Pt J, No.1. p.56, February 1988

51. B.M.A. Rhemee and J.S Davies, 'Finite-element solution of integrated optical waveguides,' IEEE J. Lightwave Technol., Vol.LT-2, p.682, October 1984

52. P. Strehe, G.P. Hove and I. Montrosset, 'Guided Modes of Ti:$LiNbO_3$ Channel Waveguides: A Novel Quasi-Analytical Technique in Comparison with the Scalar Finite-Element Method,' IEEE J. Lightwave Technol., Vol.LT-6, No.8, p.1126, June 1988

53. S.K. Ghandhi, VLSI Fabrication Principles, New York: Wiley Interscience 1983

54. M.H. Felt and J.A. Fleck, Jr., 'Comparison of calculated and measured performance of diffused channel-waveguide couplers,' J. Opt. Soc. Am., Vol.73, No.10, p.1298, October 1983

55. O. Mazumo, 'Optical electrode design for integrated optics modulator,' IEEE J. Quantum Electron., Vol. QE-18, No.3, p.393, Mar. 1982

56. O.G. Ramer, 'Integrated optic electrooptic modulator electrode analysis' IEEE J. Quantum Electron., Vol. QE-18, No.3, p.386, Mar. 1982

57. E.C. Gupta, Microstrip Lines and Slotlines, MA: Artech House, Inc., 1979

58. R.H. Wu and C.H. Chen, 'A semiar variational conformal mapping technique for weakly guiding dielectric waveguides,' IEEE J. Quantum Electron., Vol.QE-22, No.5, p.603, May 1988

59. C.N. Kim and R.V. Ramaswamy, 'Overlay integral factors in integrated optic modulators,' IEEE J. Lightwave Technol., Vol.LT-7, No.7, p.1063, July 1989,

60. T. Tamir, Topics in Applied Physics: Integrated Optics. Berlin: Springer-Verlag, 1979

61. J.P. Donnelly and A. Gopinath 'A comparison of power requirements of traveling-wave $LiNbO_3$ optical couplers and interferometric modulators' IEEE J. Quantum Electron., Vol.QE-23, No.1, p.30, January 1987

62. W.K. Burns, T.G. Giallorenzi, H.F. Taylor and E.J. West, 'Interferometric waveguide modulator with polarization-independent operation' Appl. Phys. Lett., Vol.33, No.11, p.944, 1 December 1978

63. O.L. Tangonan, D.L. Persechini, J.F. Lotspeich and K.K. Hornechi,' Electrooptic diffraction modulation in Ti-diffused $LiTaO_3$,' Appl. Optics, Vol.17, No.2H, p.3259, 15 October 1978

64. R.C. Alferness and L.L. Buhl, 'Waveguide electro-optic polarization transformer.' Appl. Phys. Lett., Vol 38, No 9, p.655, 1 May 1981

65. D.J. Elliott, Integrated circuit fabrication technology, New York: McGraw Hill, 1982

BIOGRAPHICAL SKETCH

Chang Min Kim was born in Seoul, Korea, in April, 1950. He received the B.S. and the M.S. degrees in electronics engineering from the Seoul National University, Seoul, Korea in 1975 and 1982, respectively.

He joined the Faculty of the Department of Electronics Engineering at the Seoul City University in 1983 and served as an Assistant Professor from 1985 to 1986. He was a Visiting Scholar at the University of Texas at Austin during fall semester 1986 on the Fulbright Research Grant. He has been in the Ph.D. degree program since spring semester 1987 in the Department of Electrical Engineering at the University of Florida, Gainesville, FL. His research interests include analytical treatment and fabrication of optical amplifiers and optical switches/modulators.

I certify that I have read this study and that in my opinion it conforms to acceptable standards of scholarly presentation and is fully adequate, in scope and quality, as a dissertation for the degree of Doctor of Philosophy

Ramu V. Ramaswamy, Chair
Professor of Electrical Engineering

I certify that I have read this study and that in my opinion it conforms to acceptable standards of scholarly presentation and is fully adequate, in scope and quality, as a dissertation for the degree of Doctor of Philosophy

Ramakant Srivastava
Associate Professor of Electrical Engineering

I certify that I have read this study and that in my opinion it conforms to acceptable standards of scholarly presentation and is fully adequate, in scope and quality, as a dissertation for the degree of Doctor of Philosophy

Peter Zory
Professor of Electrical Engineering

I certify that I have read this study and that in my opinion it conforms to acceptable standards of scholarly presentation and is fully adequate, in scope and quality, as a dissertation for the degree of Doctor of Philosophy

Sheng S Li
Professor of Electrical Engineering

I certify that I have read this study and that in my opinion it conforms to acceptable standards of scholarly presentation and is fully adequate, in scope and quality, as a dissertation for the degree of Doctor of Philosophy.

Joseph H. Simmons

Joseph Simmons
Professor of Materials Science
and Engineering

This dissertation was submitted to the Graduate Faculty of the College of Engineering and to the Graduate School and was accepted as partial fulfillment of the requirement for the degree of Doctor of Philosophy

August 1989

Hubert A. Beaver

Dean, College of Engineering

Dean, Graduate School